

Moving mesh cosmology: the hydrodynamics of galaxy formation

Debora Sijacki^{1*}, Mark Vogelsberger¹, Dušan Kereš^{2,3†}, Volker Springel^{4,5}, and Lars Hernquist¹

¹ *Harvard-Smithsonian Center for Astrophysics, 60 Garden Street, Cambridge, MA, 02138, USA*

² *Department of Astronomy and Theoretical Astrophysics Center, University of California, Berkeley, CA 94720-3411, USA*

³ *Department of Physics, Center for Astrophysics and Space Sciences, University of California at San Diego, 9500 Gilman Drive, La Jolla, CA 92093, USA*

⁴ *Heidelberg Institute for Theoretical Studies, Schloss-Wolfsbrunnengasse 35, 69118 Heidelberg, Germany*

⁵ *Zentrum für Astronomie der Universität Heidelberg, ARI, Mönchhofstr. 12-14, 69120 Heidelberg, Germany*

14 June 2012

ABSTRACT

We present a detailed comparison between the well-known smoothed particle hydrodynamics (SPH) code GADGET and the new moving-mesh code AREPO on a number of hydrodynamical test problems. Through a variety of numerical experiments with increasing complexity we establish a clear link between simple test problems with known analytic solutions and systematic numerical effects seen in cosmological simulations of galaxy formation. Our tests demonstrate deficiencies of the SPH method in several sectors. These accuracy problems not only manifest themselves in idealized hydrodynamical tests, but also propagate to more realistic simulation setups of galaxy formation, ultimately affecting local and global gas properties in the full cosmological framework, as highlighted in companion papers by Vogelsberger et al. (2011) and Keres et al. (2011). We find that an inadequate treatment of fluid instabilities in GADGET suppresses entropy generation by mixing, underestimates vorticity generation in curved shocks and prevents efficient gas stripping from infalling substructures. Moreover, in idealized tests of inside-out disk formation, the convergence rate of gas disk sizes is much slower in GADGET due to spurious angular momentum transport. In simulations where we follow the interaction between a forming central disk and orbiting substructures in a massive halo, the final disk morphology is strikingly different in the two codes. In AREPO, gas from infalling substructures is readily depleted and incorporated into the host halo atmosphere, facilitating the formation of an extended central disk. Conversely, gaseous sub-clumps are more coherent in GADGET simulations, morphologically transforming the central disk as they impact it. The numerical artifacts of the SPH solver are particularly severe for poorly resolved flows, and thus inevitably affect cosmological simulations due to their inherently hierarchical nature. Taken together, our numerical experiments clearly demonstrate that AREPO delivers a physically more reliable solution.

Key words: methods: numerical – cosmology: theory – cosmology: galaxy formation

1 INTRODUCTION

Numerical simulations have become an indispensable tool for studying astrophysical phenomena. Over the last decade, the numerical accuracy and fidelity of simulation methods have undergone drastic improvements, both in terms of resolvable

dynamic range and of the complexity of the physical processes that are now routinely incorporated into the codes. This remarkable progress in numerical techniques coupled with the ever increasing power of high performance computing platforms has led to major advances in a number of topics, such as star formation (Klessen et al. 2009), accretion disk dynamics and associated jet phenomena (Gammie et al. 2003; De Villiers & Hawley 2003), supernova explo-

* Hubble Fellow. E-mail: dsijacki@cfa.harvard.edu

† Hubble Fellow.

sions (Janka et al. 2007), black hole coalescence (Pretorius 2007), and cosmic structure formation (Springel et al. 2005).

Clearly, an in-depth understanding of many astrophysical processes, particularly those that are inherently non-linear, relies crucially on the accuracy and realism of the numerical approach. While the latter is largely determined by the degree of adequateness, comprehensiveness and consistency of the physical model assumed, the former depends sensitively on the discretization scheme adopted for the equations, which with increasing resolution should converge to the correct solution. Nonetheless, even for some elementary physical problems, with known analytic solutions, simulation methods can sometimes produce poorly converged results, or even converge to a solution which is, however, different from the expected result (Springel 2010b).

In the context of hydrodynamical cosmological simulations, an important example is given by the seminal work of Frenk et al. (1999) (the Santa Barbara Comparison Project). This study performed a detailed comparison between twelve different simulation codes that tracked the non-radiative evolution of a forming galaxy cluster in a cold dark matter (CDM) cosmology. The initial conditions were generated independently by each group from a provided linear theory density or displacement field. Very different numerical methods, which can be broadly classified into smoothed particle hydrodynamics (SPH) and mesh-based techniques, employing also different gravity solvers and different effective resolutions, were then used by the groups to follow the formation and evolution of the target object. Reassuringly, the Santa Barbara Comparison Project has shown that the global properties of the simulated object, both in terms of dark matter and gas distribution, were in reasonable agreement among the codes. However, detailed gas properties of the Santa Barbara cluster, notably in the central region, exhibited a much poorer level of consistency. In particular, Frenk et al. (1999) pointed out that there is a systematic discrepancy in the central entropy profiles predicted by SPH and mesh-based codes, with the former producing power-law entropy profiles all the way to the centre and the latter yielding some form of entropy core.

Even though progress in numerical techniques has led to substantial improvements in current simulation codes compared to those considered in Frenk et al. (1999), the systematic difference in the predicted central cluster entropy still persists today, and its origin has not been fully understood thus far. Agertz et al. (2007) have performed a set of numerical experiments with SPH and mesh codes, where they have simulated the evolution of a cold, dense blob in a hot windtunnel. By comparing the outcomes from different methods (and at various resolutions) against the characteristic blob disruption timescale expected analytically, they conclude that in SPH codes the development of fluid instabilities can be numerically hampered. The suppression of dynamical fluid instabilities, such as Kelvin-Helmholtz, Rayleigh-Taylor, and Richtmyer-Meshkov instabilities, leads to less efficient mixing of fluid elements with different specific entropy, and hence also inhibits entropy generation through mixing in the simulated system. In simulations of colliding isolated galaxy clusters, Mitchell et al. (2009) have shown that the central entropy profiles obtained with the SPH code GADGET and the mesh code FLASH show a similar level of

discrepancy as found by Frenk et al. (1999), which they attribute to the different levels of mixing.

There have been a number of attempts to improve the description of mixing in SPH by modifying the standard set of discretized equations (see e.g. Price 2008; Wadsley et al. 2008; Heß & Springel 2010) or by incorporating a Riemann solver in place of the artificial viscosity (e.g. Inutsuka 2002; Cha & Whitworth 2003; Murante et al. 2011). For example, Price (2008) has shown that the introduction of an artificial thermal conductivity term can improve the behavior of fluid elements at contact discontinuities, which in turn leads to better developed Kelvin-Helmholtz instabilities. More generally, Wadsley et al. (2008) suggested that a physical modeling of heat diffusion is necessary when simulating high Reynolds number flows (both for SPH and mesh-based methods), and that by applying such an approach a flat entropy core is likely a more correct solution for non-radiative galaxy cluster simulations.

Differences in the hydrodynamical solver between SPH and mesh-based codes are possibly not the only reason for the systematically different central entropy profiles in the Santa Barbara Comparison Project. As mentioned above, the groups involved in this study did not use identical initial conditions, and did not perform their simulations at equal numerical resolutions and with identical gravity solvers, which opens up the possibility of additional sources for discrepancies. A more recent code comparison study by Heitmann et al. (2008) evolved uniform, dark matter only cosmological boxes in a Λ CDM universe with 10 different codes, starting from the same initial conditions. They showed that for large systems there is a reassuring agreement in the halo mass functions between the codes, as well as in the internal structures of haloes in the outer regions. However, the study by Heitmann et al. (2008) also revealed significant discrepancies for small halos, demonstrating that the typical root grid resolution commonly adopted in adaptive mesh refinement (AMR) codes for simulations of cosmic structure formation is overly coarse and leads to a suppression of low mass halo formation (see also O’Shea et al. 2005). This emphasizes the need to simultaneously strive for high accuracy both in the gravity solver and in the hydrodynamics. Additionally to the high accuracy of the gravity and hydro solver, it is also of prime importance to adopt sufficiently high mass and spatial resolution for the studied problem at hand. For example, if besides pure hydrodynamics other physical processes, such as star formation and associated feedback, are modelled in cosmological simulations, it is necessary to resolve all star-forming haloes with a sufficiently large number of resolution elements to reach convergent results (Springel & Hernquist 2003b).

In the present work we perform a detailed comparison study between the widely used SPH code GADGET and the novel moving-mesh code AREPO on a number of hydrodynamical test problems with increasing levels of complexity. We have adopted a combination of existing test problems and newly devised numerical experiments^{*} in order to provide a clear link between the results of our test problems and

^{*} High-resolution images and movies of various numerical experiments are available for download at the website <http://www.cfa.harvard.edu/itc/research/movingmeshcosmology>

those of full cosmological simulations, which are discussed in detail in our companion papers (Vogelsberger et al. 2011, hereafter Paper I) and (Keres et al. 2011, hereafter Paper II). Our work thus contributes to the understanding of the significant differences in baryon properties found in cosmological simulations between mesh-based and SPH techniques, both at a global level (see Paper I) and at the scale of individual galaxies (see Paper II).

A unique advantage of our comparison study lies in the fact that simulations with GADGET and AREPO can be started from identical initial conditions and that both codes employ the same gravity solver. Note that in case of AREPO gravitational softenings for the gas can be kept fixed as is the case of GADGET or can be computed adaptively determined by the cell size. In the numerical experiments with gas self-gravity we explore both fixed and adaptive gas softening, where in the case of adaptive softenings a floor equal to the GADGET gas softenings is set. We find that these different choices of gravitational softenings in AREPO do not affect our findings. This allows us to isolate cleanly how the different hydro solvers used by GADGET and AREPO impact gas properties. We first consider elementary hydrodynamical numerical tests such as a strong 1D Sod shock tube test, a 2D implosion test (which is widely used for benchmarking mesh codes, but has rarely been considered in SPH), and the “blob” test (Agertz et al. 2007). We then perform a number of isolated or merging halo simulations in the non-radiative regime, aimed at understanding how shocks and fluid instabilities affect their gaseous atmospheres. Finally, we study the differences between GADGET and AREPO in radiative simulations, where we follow inside-out disk formation and interactions between the central disks and orbiting substructures.

This paper is organized as follows. In Section 2, we provide a brief overview of the numerical codes used and the types of simulations performed. Section 3 represents the core of the paper where all of our numerical experiments are discussed. Finally, we summarize our findings in Section 4.

2 METHODOLOGY

2.1 Numerical codes

2.1.1 GADGET

GADGET is a massively parallel TreePM-SPH code widely used in numerical astrophysics. In this study we adopt the latest GADGET-3 version. A detailed description of an earlier version can be found in Springel (2005). GADGET is fully adaptive in time and space, and in its entropy formulation for SPH (Springel & Hernquist 2002) manifestly conserves both energy and entropy in the absence of artificial viscosity. Gravitational forces are computed with an octtree method (Barnes & Hut 1986; Hernquist 1987). To speed up the computation, long-range forces can be optionally evaluated with a PM method, with the tree being restricted to short-range forces only.

In all our tests, we adopt as standard value for the artificial viscosity strength $\alpha = 1.0$, and we use 64 neighbours for kernel interpolation in three dimensional simulation, unless we specifically vary these parameters to assess their effect.

2.1.2 Other SPH implementations

As mentioned in the introduction, there have been a number of recent proposals to improve the standard SPH implementation in various ways, for example by invoking a time-dependent artificial viscosity (Morris & Monaghan 1997; Dolag et al. 2005), a modified density estimate (e.g. Ritchie & Thomas 2001; Heß & Springel 2010; Saitoh & Makino 2012), a decoupling of the hot and cold neighbours in multiphase flows (Marri & White 2003; Okamoto et al. 2003), an artificial thermal conductivity (Price 2008), a modified equation of motion (Heß & Springel 2010; Abel 2011), an explicit modelling of mixing (Wadsley et al. 2008), an enlarged neighbour number combined with a different kernel shape (Read et al. 2010), or a replacement of the artificial viscosity by a Riemann solver (e.g. Inutsuka 2002; Cha & Whitworth 2003; Murante et al. 2011). While some of these modifications of the standard SPH formalism deliver more accurate results in targeted numerical experiments, no consensus has yet emerged whether any of these approaches (or a combination thereof) is sufficiently robust for cosmological applications and leads to universally more accurate results in galaxy formation simulations. Therefore, in this work we focus on the traditional SPH implementation rather than on the various possible modifications proposed recently. We note that this standard formulation of SPH has also been typically employed in state-of-the-art cosmological SPH calculations (e.g. Crain et al. 2009; Di Matteo et al. 2012). Furthermore, as discussed in Paper I, there are other, generic issues with SPH that have not been resolved by any of the above modifications. These issues ultimately mean that SPH does not currently have a formal convergence condition, which also complicates rigorous evaluations of variants of the standard SPH algorithm.

2.1.3 AREPO

AREPO (Springel 2010a) is a new massively parallel simulation code, which uses the same gravity solver as GADGET (augmented with the possibility of adaptive gravitational softenings for the gas), but employs a completely different method for the evolution of the fluid. It adopts a second-order accurate finite volume technique, where the solution of the Euler equations is computed by an unsplit Godunov method equipped with an exact Riemann solver. Throughout we use the default choice of the slope limiter in AREPO which prevents the linear reconstruction to over- or undershoot the maximum/minimum values of neighbouring cells, as described in detail in Springel (2010a). Unlike standard finite-volume codes used in numerical astrophysics, AREPO solves the equations on an unstructured Voronoi mesh, which is allowed to freely move with the fluid. The resulting quasi-Lagrangian nature of AREPO automatically guarantees spatial adaptivity and greatly reduces numerical diffusivity even in the presence of large bulk flows. Compared to standard Eulerian mesh codes, AREPO has the advantage of being fully Galilean invariant (as is GADGET as well), it is less prone to advection errors and over-mixing, and preserves contact discontinuities better.

In this study, we employ a mesh regularization method[†] in AREPO by default, based on a Lloyd algorithm (for details see Springel 2010a), which ensures that the geometric centre of each Voronoi cell is sufficiently close to the cell's mesh-generating point to ensure good accuracy of the spatial reconstruction. In cosmological simulations (see Paper I), an alternative regularization criterion has proven to be advantageous, based on the maximum opening angle under which a cell face is seen from the mesh-generating point. We have checked for a number of test runs presented in this study that this alternative regularization method does not affect any of the results described here.

For most of the simulations presented here we do not use the possibility of mesh refinement and de-refinement operations (see Springel 2010a), except in our numerical experiments with star formation presented in Section 3.4.3, where we employ it for verification of our findings. Mesh de-/refinements are used to constrain the mass of cells to a small range around a target value (equal to the gas particle mass in the matching GADGET run). This restricts the spectrum of star particle masses which are generated from gaseous cells, and thus assures that N-body heating effects are minimized. Also, as our default choice we use the energy formulation of AREPO. We verified for each numerical experiment that there is no significant spurious transfer of kinetic into thermal energy.

2.2 Types of simulations

2.2.1 Physical processes

We perform both radiative and non-radiative hydrodynamical simulations, where in the former case gas is represented by a primordial mixture of hydrogen and helium in an optically thin limit (Katz et al. 1996). In simulations with radiative cooling, we employ a subresolution multi-phase model for star formation and associated supernova feedback (Springel & Hernquist 2003a). We slightly modify the behaviour of this model for gas elements which are hot but already above the density threshold for star formation, by allowing them to settle quickly onto the effective equation of state: if their newly estimated temperature from radiative cooling would fall below the temperature of the multiphase medium, we set it equal to the multiphase temperature. This change has been introduced to make the sub-grid star formation module consistent with its current implementation in AREPO. We also perform some simulations with the subresolution star formation model where spawning of star particles is intentionally prevented, but the cold, dense gas above the density threshold for star formation is still governed by the effective equation of state. These simulations are particularly useful for understanding the development of dynamical instabilities between cold and hot media, and have the advantage of not being prone to fragmentation which might affect pure cooling runs.

Note that we deliberately consider only very simplified baryonic physics implementations in all presented numerical experiments, as detailed above. This is for two reasons.

First, we need to make sure that gas cooling and star formation processes are treated on an as equal footing as possible in order to allow a meaningful comparison of the two codes. Thus, we adopt a simple multi-phase model for star formation which is largely insensitive to the detailed structure of the gas on very small scales where gas joins the interstellar medium and is described by a relatively stiff effective equation of state. Second, our aim is to isolate in an as clean manner as possible the differences between simulated systems with GADGET and AREPO stemming from the discretization of the fluid equations alone. This goal is given precedence over trying to reproduce observational findings through a more sophisticated modelling of additional physics. While it is likely that such additional physical processes will change the properties of some of our simulated systems by possibly different degrees in GADGET and AREPO, it is of significant interest in its own right to disentangle numerical uncertainties from uncertainties in the physical modelling of star formation and associated feedback processes.

2.2.2 Gravitational softenings

For simplicity, many of the numerical experiments presented in this study have been evolved without gas self-gravity. For simulations where self-gravity of the gas is nevertheless included, we note that GADGET employs constant gravitational softening for gas particles in the manner of Hernquist & Katz (1989), while AREPO uses either the same constant gravitational softening or an adaptive softening determined by the cell size with a minimum softening value set to the fixed softening of the matching GADGET run. We have verified that this does not lead to substantial differences for any of the tests presented in this study.

2.2.3 Effective hydro resolution

Even though GADGET and AREPO calculations use the same gravity solver and can be initiated from identical initial conditions, due to the very different nature of the hydro solver it is not straightforward to define unambiguously a comparison strategy at the same or equivalent hydro resolution. In this study we choose to keep the number of resolution elements the same in the both codes, i.e. to have the same number of SPH particles as Voronoi cells, corresponding to a comparable mass resolution in the gas. This allows us to adopt indeed the same initial conditions and to also have similar mass resolution in the stellar component in those simulations where star formation is included. Furthermore, the CPU costs of the two codes are then roughly comparable, as discussed in Paper I.

We note, however, that this choice implies that the “effective” spatial resolution of GADGET is lower than that of the matching moving-mesh calculation, given that fluid properties in SPH are evaluated by kernel averaging over a somewhat larger number of neighbours than needed in AREPO for its stencil of neighbouring cells, for example for gradient estimates. For this reason, we perform all of our numerical experiments at a number of different resolutions, which also help us to gain some insight into the convergence properties of the two codes. Nonetheless, it is important to

[†] Note that in the presence of mesh regularization the Galilean invariant nature of the AREPO code is not violated.

stress that the convergence properties of the SPH method are still not well understood. For example, one would ultimately require that the number of neighbours be increased with increasing total particle number (see e.g. Rasio 2000; Read et al. 2010; Robinson & Monaghan 2011, and discussion in Paper I), but the appropriate scaling of the neighbour number with increasing resolution is currently unknown. It is common practice, which we adopt as well, to simply always keep the number of neighbours fixed when the total particle number is varied, even though the discretized representation of the density field is not guaranteed to converge to its underlying smooth distribution with this choice.

2.3 Initial conditions generation

For all the tests presented in this study (except for the “blob” experiment of Agertz et al. 2007, for which we take publicly available initial conditions) we generate the initial conditions in terms of simple particle/point distributions. Depending on the simulated problem at hand, we either populate the simulated domain with particles uniformly spaced on a regular lattice or we adopt Poisson sampling of a density field. For simulations with AREPO, the positions of particles in the initial conditions define mesh generating points. All purely hydrodynamical numerical experiments have been performed with periodic initial conditions. In the case of simulated problems where we follow the evolution of an isolated gaseous halo or merging haloes, we select vacuum boundary conditions for GADGET. In simulations with AREPO, it is however necessary to enclose the simulation in a finite volume in order to make the tessellation with a mesh well posed. If needed, we thus add a low resolution background grid to our initial conditions, which is chosen sufficiently large as to encompass the spatial extent of our simulated objects at all times. The procedure adopted for this background grid generation, which also reduces the Poisson noise in the initial mesh geometry, is described in detail in Section 9.4 of Springel (2010a).

3 RESULTS

3.1 Strong shocks and interacting curved shocks in multi-dimensions

3.1.1 Strong shock in 1D

As an introductory problem, we consider a strong shock with a Mach number $M = 6.3$ in one dimension. The initial conditions have been constructed as follows: in a computational domain of length $L_x = 10.0$, $N = 200$ particles (cells) have been placed on a regular grid such that for $x < 5.0$ the pressure and density are $P = 30.0$, $\rho = 1.0$, while for $x \geq 5.0$ they are $P = 0.14$ and $\rho = 0.125$, respectively. We adopt an adiabatic index $\gamma = 1.4$, and assume that the fluid is initially at rest. In the test run with GADGET, we adopt a standard value of the artificial viscosity equal to $\alpha = 1.0$, and we vary the neighbor number N_{ngb} by setting it to 5, 7, 11, or 15, appropriate for the 1D nature of the test.

In Figure 1, we show the gas density, velocity, entropy (i.e. P/ρ^γ) and pressure at time 0.25 for GADGET with $N_{\text{ngb}} = 5$ (left-hand panels), and for AREPO (middle

panels). Blue symbols give the values of individual particles/cells, dashed red lines represent the initial conditions, while dotted red lines are the analytic solution to this Riemann problem. It can be seen that in both GADGET and AREPO the post-shock properties of the fluid are captured well, but the shock and the contact discontinuity are significantly broader in GADGET which also shows a characteristic ‘pressure-blip’ at the contact discontinuity (see also Springel 2010b). Contrary to what one may perhaps suppose, the post-shock oscillations present in GADGET are not caused by inadequate artificial viscosity, but are instead induced by an inaccurate treatment of the sharp contact discontinuity of the initial conditions. To demonstrate this point, we have performed exactly the same shock tube test but this time smoothing the initial contact discontinuity over 5 particles in density and internal energy with a Hann window function, so as to reduce its sharpness. Green cross symbols in the third row of Figure 1 (see also the right-hand panels where we zoom into the region around the shock) illustrate how the gas entropy is affected by this choice of smoothed initial conditions. Post-shock oscillations and the “spike” in entropy at the contact discontinuity are greatly reduced.

It is interesting to note that also in the case of AREPO the “spike” in the entropy at the contact discontinuity is cured by our smoothed initial conditions. This feature is absent in the results of standard grid codes, as we have verified by running this test with a static mesh option in AREPO (and by running it with ENZO), which tends to broaden contact discontinuities (depending on the advection speed) and thus largely wash-out this feature. This can be seen in the lower right-hand panel of Figure 1 where we show the results from the AREPO run with a static mesh with magenta triangle symbols. The much lower numerical diffusivity of AREPO for contact discontinuities preserves the initial start-up feature to much higher accuracy, but at the same time this can lead to a larger ‘wall heating’ effect (Rider 2000) than in static grid codes, which tend to smooth out at some level the initial start-up errors at the contact discontinuity (see also the description of the Noh problem in Springel 2010a).

When we increase the number of neighbors from $N_{\text{ngb}} = 5$ (as shown in Figure 1) to 15 in the shock tube tests performed with GADGET (but keeping the total number of particles constant), the spatial region over which the contact discontinuity and the shock are broadened increases progressively, but the pressure jump between the post-shock and pre-shock gas outside of the broadened region remain the same, yielding consistent Mach numbers. Based on these tests we later discuss in more detail the consequences of shock broadening in GADGET when simulating the radial infall of gas into static dark matter haloes in Section 3.3.2.

3.1.2 Interacting shocks in 2D

While one-dimensional shock tube tests are an essential basic benchmark for hydrodynamical code performance, they are far less demanding than multi-dimensional flow where complex interactions of non-planar shocks may occur, as is the case in realistic structure formation simulations. Such tests have however not been examined widely in the SPH literature thus far. We hence perform the so-called “implosion

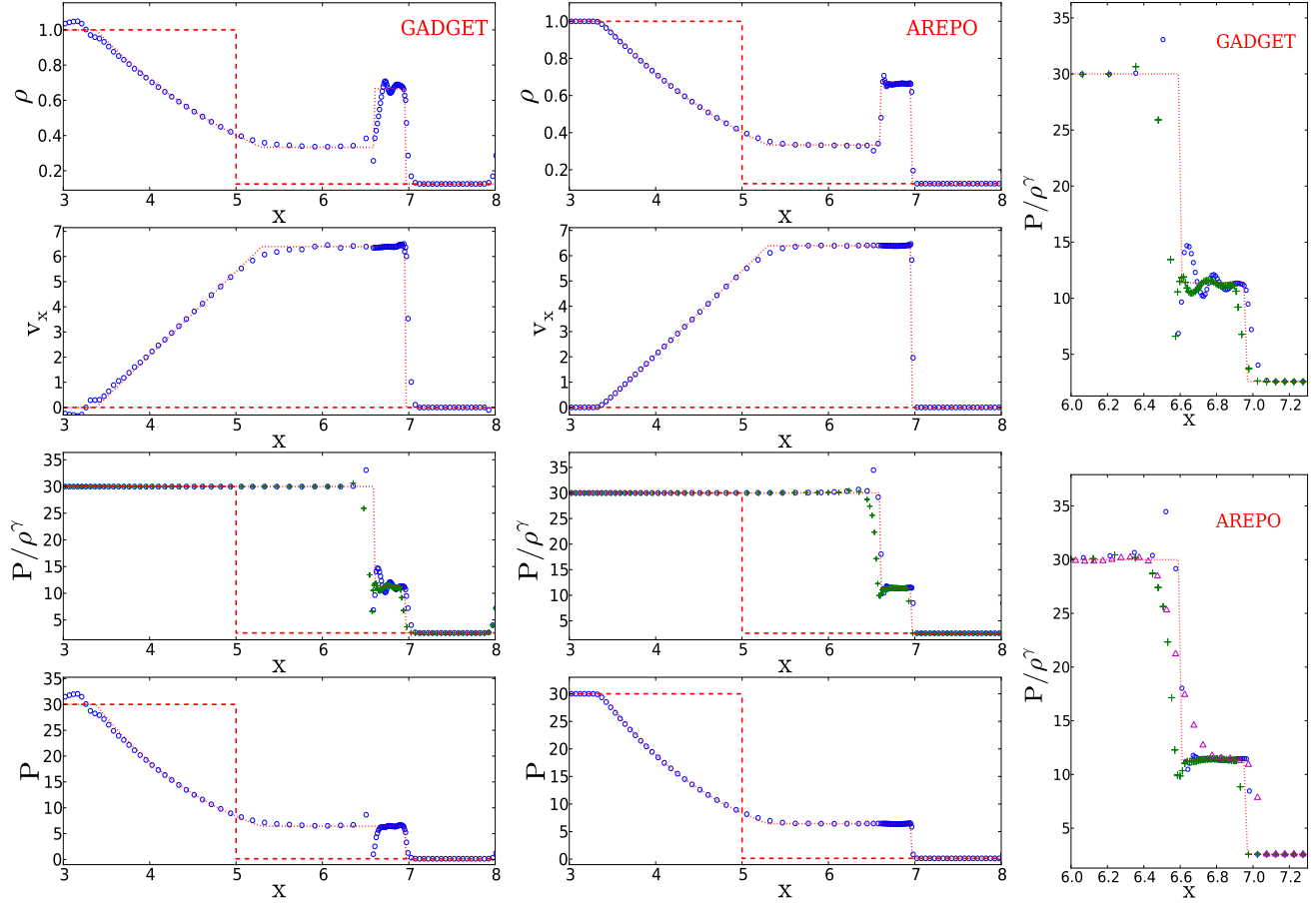


Figure 1. One dimensional shock tube problem with Mach number $M = 6.3$ at time $t = 0.25$. Left-hand panels: GADGET with standard artificial viscosity $\alpha = 1.0$ and $N_{\text{ngb}} = 5$. Middle panels: AREPO with moving mesh. Dashed red lines denote initial conditions, while dotted red lines represent the analytic solution. In the third row, green cross symbols illustrate gas entropy in a shock tube of the same strength but with initially smoothed contact discontinuity adopting a Hann window. Right-hand panels: zoom into the entropy profile around the shock - here magenta triangle symbols in the lower panel are for the AREPO run with a static mesh.

test” in two dimensions (Hui et al. 1999)[‡]. To set up this test problem, we select a computational domain $L_x = L_y = 0.3$ with $N_x = N_y = 200$ particles or cells, respectively (we have also run higher resolution versions with $N_x = N_y = 400$ and 800). The initial pressure and density are $P = 1.0$ and $\rho = 1.0$ for $x + y > 0.15$, while $P = 0.14$ and $\rho = 0.125$ otherwise. The adiabatic index is $\gamma = 1.4$ and the fluid is initially at rest. We performed this test with GADGET adopting an artificial viscosity of $\alpha = 1.0$ and $N_{\text{ngb}} = 22$ smoothing neighbours (suitable for this 2D test). While previously this test has been considered using reflective boundary conditions, we here adopt periodic boundary conditions due to their more straightforward implementation in SPH codes.

In Figure 2, we show density maps for simulations performed with GADGET (left-hand panels) and with AREPO (right-hand panels), at times $t = 0.1, 0.3, 0.5$ and 0.7 for $N_x = N_y = 200$. The complex, evolving gas density

structure is caused by the continuous interaction of shocks throughout the computational domain. Initially, due to the discontinuity in density and pressure along $x + y = 0.15$, a planar mild shock front develops perpendicular to the $x = y$ diagonal traveling towards the origin. Given that we have adopted periodic boundary conditions, the gas will interact on all four sides of the simulated box, and in particular, interacting shock waves in the lower left-hand corner result in the formation of a narrow jet along the $x = y$ diagonal (which is clearly visible only in the AREPO run). As the traveling shocks accelerate the fluid in the regions of density discontinuity a Richtmyer-Meshkov instability develops, as manifested by “mushroom-like” features in the gas distribution.

While the global gas density distribution in Figure 2 agrees reasonably well in GADGET and AREPO runs (i.e. with respect to the shape of the regions with different densities and the magnitude of the density differences), there are several significant differences: *i*) shocks and contact discontinuities are much sharper in AREPO, in agreement with our findings in Section 3.1.1; *ii*) the density distribution in GADGET appears not only smoothed out, but it is also noisier, as evidenced by the graininess of the density maps, which is caused by intrinsic noise in multidimensional flows in SPH

[‡] See also “Comparison of Several difference schemes on 1D and 2D Test problems for the Euler equations” by Liska, R. and Wendroff, B., on <http://www.troja.fjfi.cvut.cz/~liska/CompareEuler/compare8/> and <http://www.astro.princeton.edu/~jstone/Athena/tests/>.

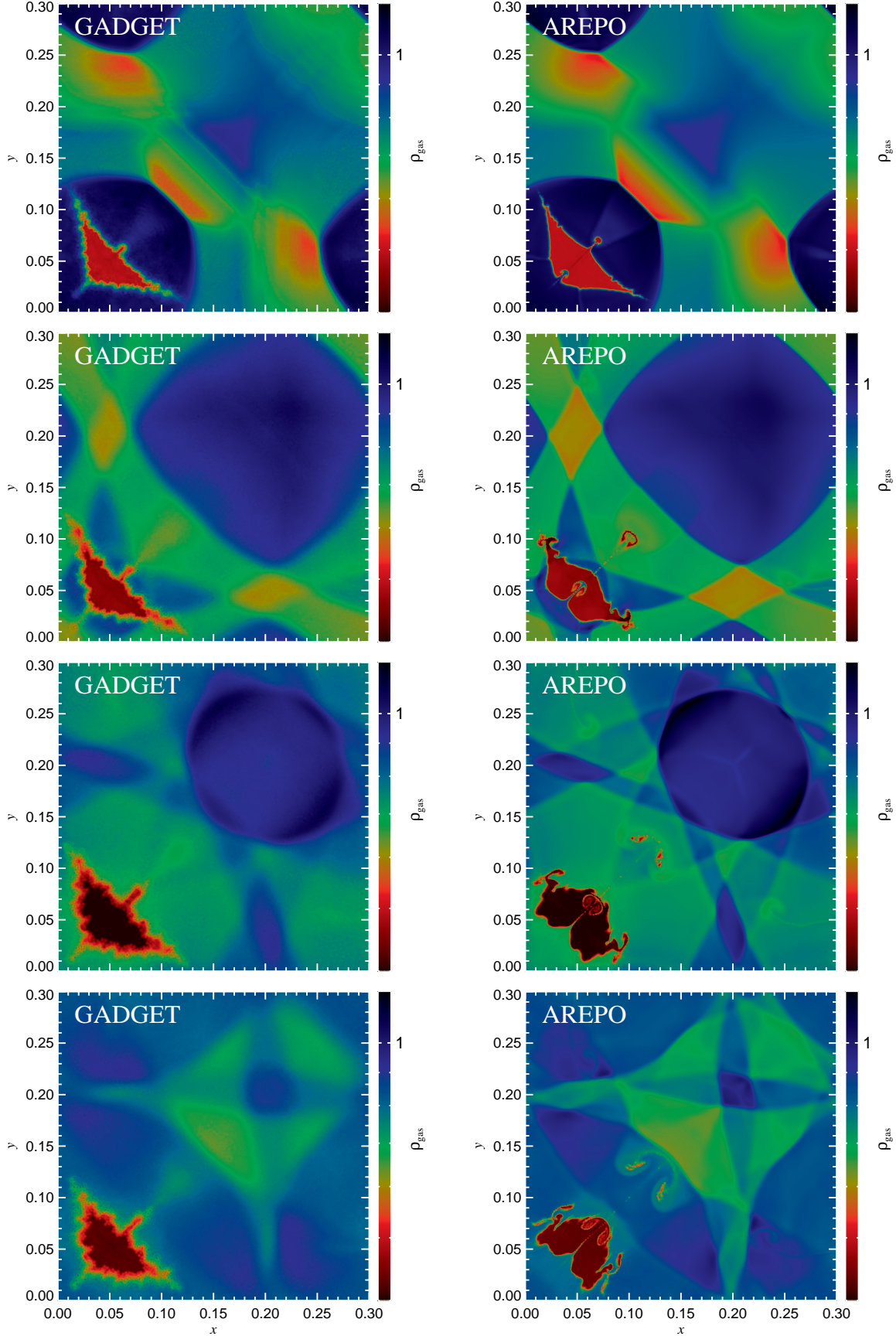


Figure 2. Implosion test in 2D at times $t = 0.1, 0.3, 0.5$ and 0.7 . Left-hand panels: GADGET ($\alpha = 1.0$, $N_{\text{ngb}} = 22$). Right-hand panels: AREPO moving-mesh. For each row, the density scale is the same in the left-hand and right-hand panels, covering the following density range: $\rho_{\text{gas}} = 1.2 - 0.4$.

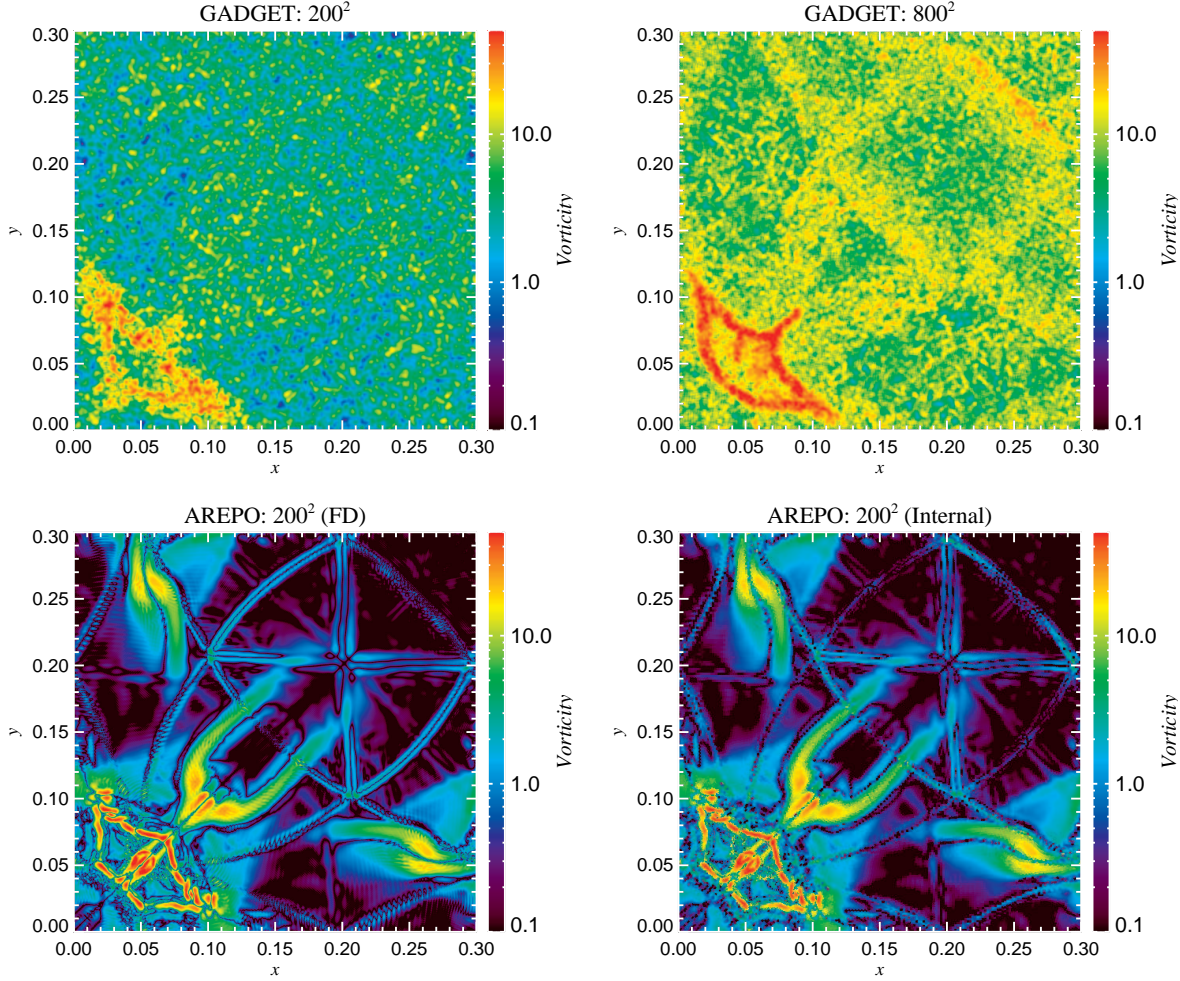


Figure 3. Vorticity maps of the implosion test in 2D at time $t = 0.3$. Upper panels: GADGET runs at two different resolutions with $N_x = N_y = 200$ (left-hand panel) and $N_x = N_y = 800$ (right-hand panel). For both resolutions, vorticity maps are computed by finite differencing the velocity field. Lower panels: vorticity maps of the AREPO run with $N_x = N_y = 200$ computed by finite differencing the velocity field (left-hand panel), and by calculating vorticity in the code based on a discretized curl-operator directly applied to the Voronoi cells (right-hand panel).

(Springel 2010b); *iii*) most strikingly, perhaps, is the quite different appearance of the low density gas in the bottom left corner – a narrow, extended, dense jet along the diagonal is largely absent in GADGET (due to the broadening of the contact discontinuity) and Richtmyer-Meshkov instabilities along discontinuities are suppressed. We have verified that higher resolution simulations with GADGET ($N_x = N_y = 400$ and 800) result in sharper shocks and contact discontinuities (with a somewhat feeble jet forming), but they cannot satisfactorily cure the absence of well-developed Richtmyer-Meshkov instabilities. This is in agreement with previous studies (e.g. Agertz et al. 2007; Springel 2010b) indicating fundamental limitations of the SPH method in its widely used form. We also note that the moving mesh in AREPO does an excellent job of maintaining symmetry across the $x = y$ diagonal. Furthermore, the level of numerical diffusion of discontinuities is very low, as indicated by the narrowness and length of the jet.

In addition to the density fields it is also instructive to analyze the vorticity distribution in the implosion test,

as shown in Figure 3. To construct vorticity maps we either *i*) first compute spatially adaptive velocity field maps for each component on a uniform grid (in our case only x and y components) and then finite difference them to obtain the curl or *ii*) we compute spatially adaptive vorticity maps, where the curl has been evaluated directly in the code. For GADGET runs, vorticity maps computed with method *i*) are shown in the upper panels of Figure 3 for $N_x = N_y = 200$ and $N_x = N_y = 800$. Using method *ii*) vorticity maps look essentially the same. In the case of AREPO (shown in the lower panels for the same run with $N_x = N_y = 200$) the vorticity maps are also very similar when computed with method *i*) or *ii*). However, regardless of the exact details of the vorticity map generation there are marked differences in the vorticity field between GADGET and AREPO. For the $N_x = N_y = 200$ run, the vorticity map in GADGET is largely featureless and noisy, with artificial suppression of vorticity generation at locations where surfaces of constant density and of constant pressure are not aligned (i.e. baroclinic source term $\propto \nabla \rho \times \nabla p$). Strikingly, even in the case

of the high resolution GADGET run with $N_x = N_y = 800$ (upper right-hand panel) vorticity generation in the regions with large baroclinic term is largely suppressed compared to the AREPO simulation, even though the latter has a much smaller number of resolution elements. It is also worth noting that the overall magnitude of the vorticity is relatively high in GADGET with respect to AREPO in the regions which should be characterized by having low vorticity. This is due to the noise alluded to above, visible both in the density and vorticity maps. This noise is inherently present in multidimensional SPH simulations. It is caused by inaccurate pressure gradient estimates and is particularly evident in the subsonic regime (for further details see e.g. Springel 2010b; Bauer & Springel 2012). The jitter in gas velocities caused by the noisy gradient estimates introduces an artificial vorticity ‘floor’ throughout the simulated volume of the box. The poor treatment of vorticity in GADGET has also direct consequences for the effectiveness of the widely used Balsara switch (Balsara 1995) for artificial viscosity which relies on evaluation of velocity divergence and curl.

Hence, from the results of the “implosion test” we conclude that while GADGET can accurately capture the main fluid properties in the case of dynamically interacting shocks with complicated geometries, there are systematic biases in detailed aspects, related to the development of fluid instabilities and to the level of fluid mixing at different entropies. These unwanted features lead to the suppression of angular momentum transport by vortices and to the damping of turbulence in the wake of curved shocks (see also Bauer & Springel 2012).

3.2 Dynamical fluid instabilities

3.2.1 Blob experiment

Our findings from the implosion test (Section 3.1.2) indicate that there are fundamental differences in the treatment of fluid instabilities between GADGET and AREPO. To investigate this issue in detail, we first consider the so-called “blob” test as proposed by Agertz et al. (2007), which has been analyzed with many different codes by now (Ageritz et al. 2007; Heß & Springel 2010; Murante et al. 2011). The idea behind this test is to simulate the evolution of a dense cold blob immersed in a hot windtunnel, mimicking in a simplified way the motion of a satellite galaxy through the intracluster medium (see also Heß & Springel 2011). If the relative velocity between the blob and the surrounding medium is supersonic, a bow shock will develop in front of the blob. Additionally, dynamical instabilities (mostly of Kelvin-Helmholtz and Rayleigh-Taylor type) will grow in the subsonic part of the flow between the bow shock and the surface of the blob (see Agertz et al. 2007, for a detailed description). These instabilities will greatly influence the evolution of the blob, leading to its eventual disintegration on the characteristic Kelvin-Helmholtz timescale set by the initial conditions.

To simulate this problem, we adopt the initial conditions used in the original Agertz et al. (2007) paper, which are publicly available[§]. The simulated domain consists of a periodic box with extensions $L_x = 2000$ kpc,

$L_y = 2000$ kpc, $L_z = 8000$ kpc, and the blob is initially placed at $x_c = y_c = z_c = 1000$ kpc. The blob has a radius $R_{\text{blob}} = 197$ kpc, and it is ten times colder and denser than the surrounding medium, such that pressure equilibrium is ensured. The density and temperature of the external medium is $\rho_{\text{medium}} = 3.13 \times 10^{-8} \text{M}_{\odot} \text{kpc}^{-3}$ and $T_{\text{medium}} = 10^7$ K, respectively, and it is moving with a constant velocity $v_{\text{medium}} = 1000 \text{km s}^{-1}$ along the z -axis. The adiabatic index is set to $\gamma = 5/3$. Following Agertz et al. (2007), we define the characteristic Kelvin-Helmholtz timescale as $t_{\text{KH}} = 1.6 t_{\text{cr}}$, where t_{cr} is the blob crushing time defined as $t_{\text{cr}} = 2R_{\text{blob}}(\rho_{\text{blob}}/\rho_{\text{medium}})^{1/2}/v_{\text{medium}}$. For these initial conditions, the characteristic Kelvin-Helmholtz timescale is $t_{\text{KH}} \sim 1.98$ Gyr.

We have performed the blob test at three different resolutions with GADGET and AREPO. The resolutions used are: $32 \times 32 \times 128$, $64 \times 64 \times 256$, and $128 \times 128 \times 512$. The two higher resolutions correspond exactly to the resolution of the simulations used in Agertz et al. (2007), while we constructed the initial conditions for the lowest resolution run by sub-sampling.

In Figure 4 we show projected surface density maps of a thin slice ($\Delta y = 100$ kpc) centred around the blob position. Left-hand panels illustrate GADGET runs at times $t = t_{\text{KH}}$, $t = 2t_{\text{KH}}$ and $t = 3t_{\text{KH}}$, while the right-hand panels are for the simulations with AREPO in the moving mesh mode. The position and the shape of the bow shock are rather similar between GADGET and AREPO runs, especially at early times, but the shock is broader and less crisp in GADGET. In the run with GADGET, the blob acquires a cap-like appearance caused by the internal shock which compresses it, and it undergoes continuous ablation due to the low pressure region which forms in the wake of the blob (Ageritz et al. 2007). While initially the blob evolution is similar in AREPO, after $t = t_{\text{KH}}$ well developed Kelvin-Helmholtz and Rayleigh-Taylor instabilities lead to an efficient shredding of the blob, mixing it with the external medium. In Figure 5 we also show projected surface density maps centred around the blob position for the $32 \times 32 \times 128$ and $64 \times 64 \times 256$ runs at $t = 3t_{\text{KH}}$.

We quantify the time evolution of the blob in Figure 6. Here we show the remaining blob mass fraction as a function of time, where the material associated with the blob is selected such as to satisfy: $T < 0.9 T_{\text{medium}}$ and $\rho > 0.64 \rho_{\text{blob}}$, as has been done in the previous studies. We compare GADGET and moving-mesh AREPO simulations, performed at three different resolutions (as indicated on the legend). While for our highest resolution runs there is a broad agreement between GADGET and AREPO for $t < t_{\text{KH}}$, blob mass fractions are systematically different afterwards. This is exactly when the transition in the mass loss rate from the ablation-dominated to the fluid instability dominated regime occurs. In the latter regime, AREPO clearly delivers a physically more trustworthy solution. The moving-mesh AREPO simulation agrees qualitatively very well with the outcome of Eulerian grid codes studied in Agertz et al. (2007). However, as noted by Springel (2011), there is a small but systematic difference with the moving-mesh code delivering slightly higher remaining blob mass for $t > 1.5 \times t_{\text{KH}}$. As expected, the GADGET simulation results agree well with the findings of Agertz et al. (2007) for the other SPH codes. This indicates that the inaccuracy

[§] <http://www.astrosim.net/>

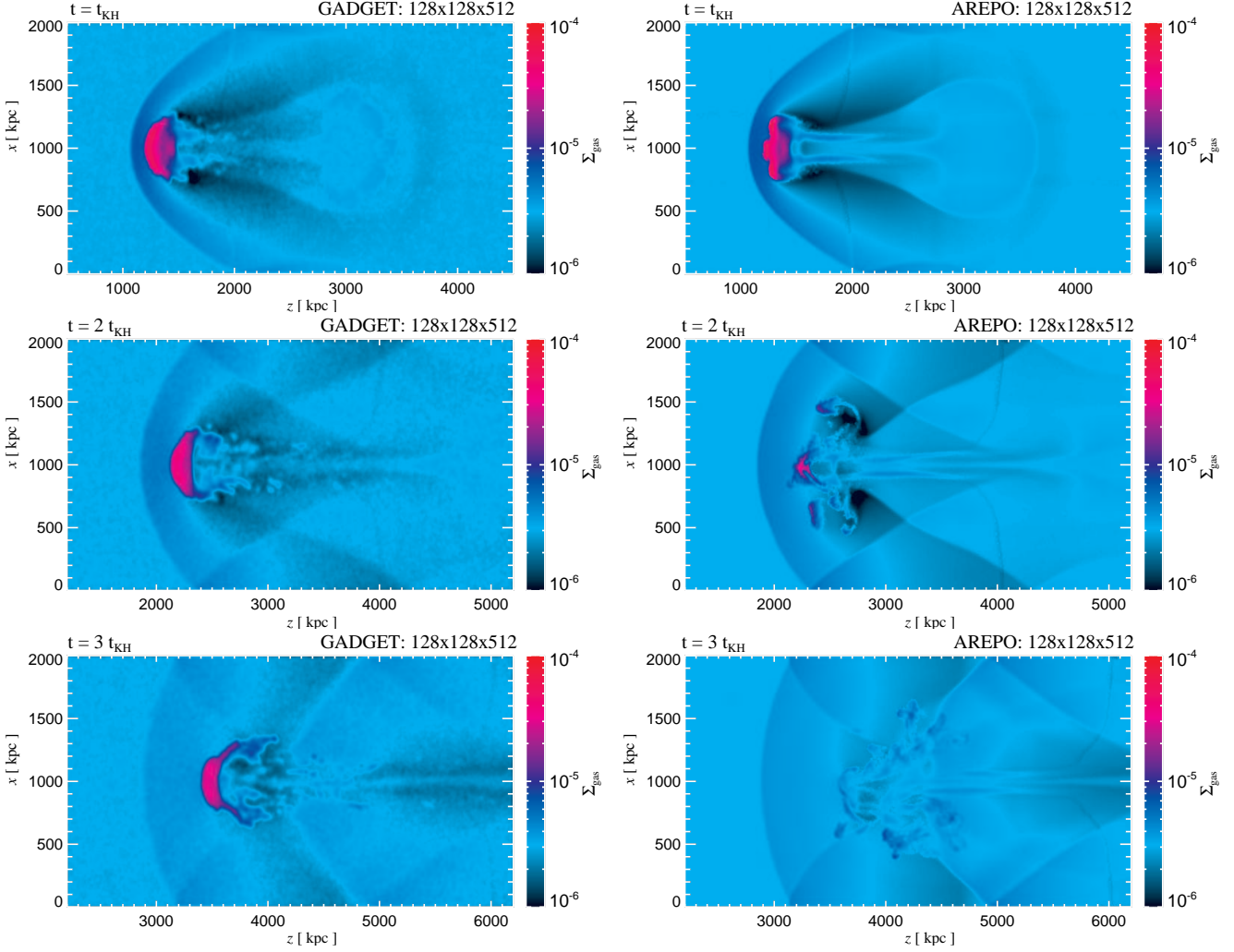


Figure 4. Projected surface density maps in units of $[M_{\odot} \text{kpc}^{-2}]$ at times $t = t_{\text{KH}}$ (top row), $t = 2 t_{\text{KH}}$ (middle row) and $t = 3 t_{\text{KH}}$ (bottom row) for GADGET (left-hand panels; $\alpha = 1.0$, $N_{\text{ngb}} = 64$) and AREPO (right-hand panels; moving mesh). The thickness of the slices is $\Delta y = 100 \text{ kpc}$, and they are centred on $y_c = 1000 \text{ kpc}$. Dynamical fluid instabilities are responsible for blob shredding on the characteristic Kelvin-Helmholtz timescale in the case of AREPO, but they are artificially suppressed in the run with GADGET, prolonging the survival time of the blob.

cies we find for GADGET are inherent to the standard SPH method, and have prompted a number of works suggesting possible improvements to the SPH method (e.g. Price 2008; Wadsley et al. 2008; Heß & Springel 2010; Saitoh & Makino 2012, see also Section 2.1.2).

3.3 Shocks and fluid instabilities in isolated halo models

3.3.1 Isolated haloes in hydrostatic equilibrium

To explore more directly the impact of shocks and fluid instabilities in the context of structure formation, we have devised a number of idealized test problems involving isolated halo models. Here we briefly describe how we set up and verify hydrostatic equilibrium configuration of the initial conditions, which form the backbone for a series of numerical experiments discussed in Sections 3.3 and 3.4.

The initial conditions are constructed by populating static or live dark matter potentials with gas particles, whose

positions are drawn randomly. For the dark matter distribution we assume a Hernquist profile (Hernquist 1990) so that we can easily generate self-consistent models when we use live haloes. The gas density profile traces the dark matter at large radii but is slightly softened in the centre, i.e.

$$\rho_{\text{gas}}(r) = \frac{M_{\text{vir}}}{(2\pi a^3)(x + x_0)(x + 1)^3}, \quad (1)$$

where M_{vir} is the virial mass of the system, a is the Hernquist scale length parameter, $x = r/a$, and $x_0 = 0.01$ is the softening scale length parameter for the gaseous halo. For the simulations without any net rotation, the initial gas velocities are set to zero, while for the simulation with non-vanishing angular momentum we assign gas velocities such that the halo is characterized by the dimensionless spin parameter

$$\lambda = \frac{J|E|^{1/2}}{GM_{\text{vir}}^{5/2}}, \quad (2)$$

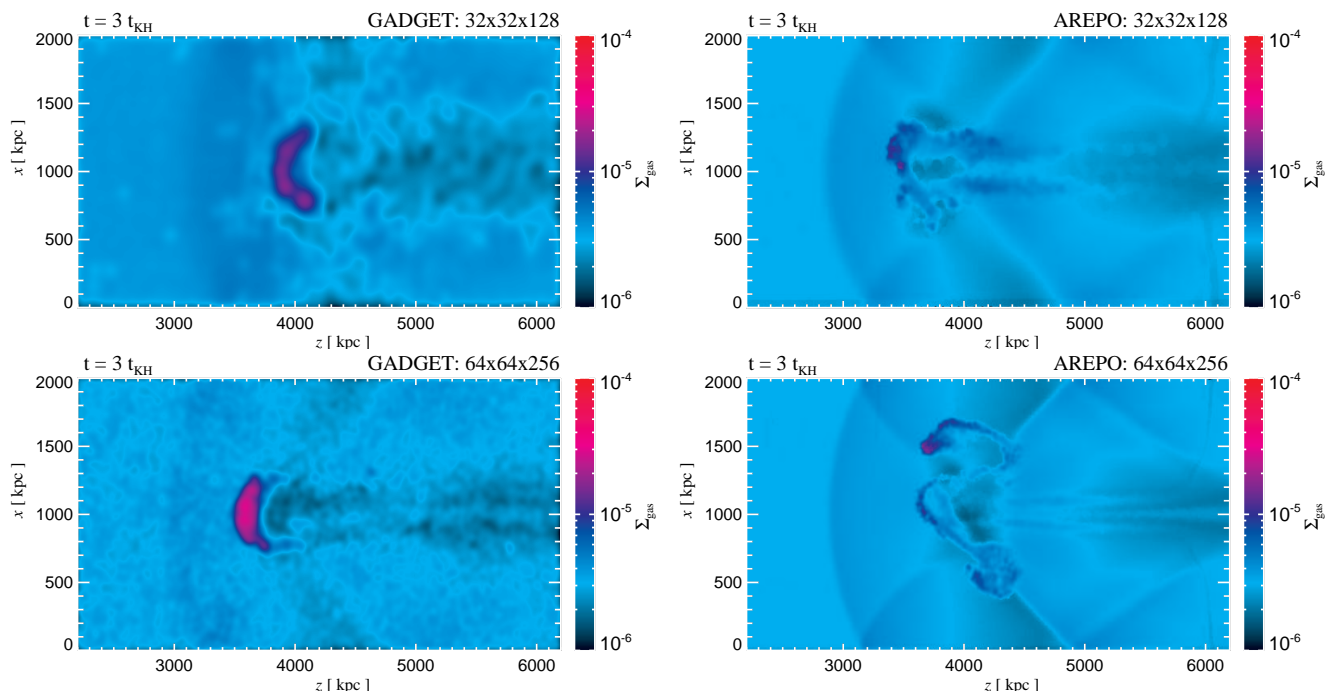


Figure 5. Projected surface density maps in units of $[M_{\odot} \text{kpc}^{-2}]$ at $t = 3 t_{\text{KH}}$ for the low (top row) and intermediate resolution simulation (bottom row) with GADGET and AREPO. The thickness of the slices is $\Delta y = 100 \text{ kpc}$ and they are centred on $y_c = 1000 \text{ kpc}$. Even at our lowest resolution, AREPO captures the dynamical evolution of the cold blob much more accurately.

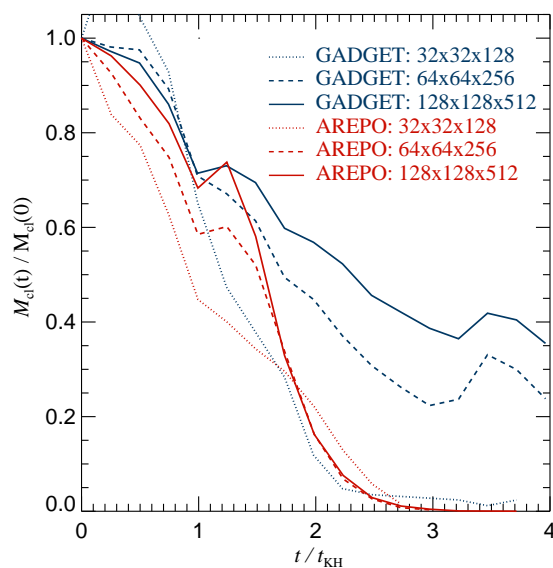


Figure 6. The remaining blob mass fraction as a function of time in units of t_{KH} . GADGET and AREPO results at three different resolutions are shown, as indicated in the legend.

where J represents the angular momentum, E is the total energy of the halo, and we assume solid body rotation.

For validation purposes we evolve isolated haloes with GADGET and AREPO for 2.45 Gyr with gas self-gravity and no radiative losses. These test runs confirm that the gas is in very good hydrostatic equilibrium within the dark matter potential. The differences in gas density, temperature and

entropy between GADGET and AREPO are within a few percent throughout the whole halo at the final time in the case of static dark matter haloes (see Figure A1 in Appendix A; for live haloes see Section 3.5).

We also observe that even though the initial gas velocities are zero (in the case with $\lambda = 0$) some small gas velocities develop over time ($\sigma_{\text{gas},3\text{D}} \sim 30 \text{ km s}^{-1}$). This is primarily caused by the initial Poisson sampling of gas positions, which implies an initial state that is not perfectly relaxed. While this numerical artifact could be avoided by explicitly relaxing the initial conditions, we note that these residual gas velocities do not have any significant bearing on our results: the total gas kinetic energy E_{kin} is less than 0.005 of either the total potential or the total internal gas energy at the final time, as shown in Figure A2 in Appendix A. It is, however, interesting to note that while the total σ_{gas} is very similar between GADGET and AREPO, there are some systematic differences in the radial profiles of σ_{gas} , which are caused by dissipation of gas motions on different spatial scales (see bottom panel of Figure A1).

3.3.2 Radial collapse of cold gas in a static dark matter halo

We now analyze how differences in shock capturing between GADGET and AREPO affect the radial infall of gas in dark matter haloes, a problem of direct cosmological interest. For this purpose we intentionally adopt a set-up as simple as possible in order to isolate differences between the codes driven by the shock treatment only. We initially set up gas in hydrostatic equilibrium and at rest within a static Hernquist potential with mass $M_{\text{vir}} = 10^{14} M_{\odot}$, scale length $a = 176 \text{ kpc}$, and a gas fraction of $f_{\text{gas}} = 0.17$. We consider

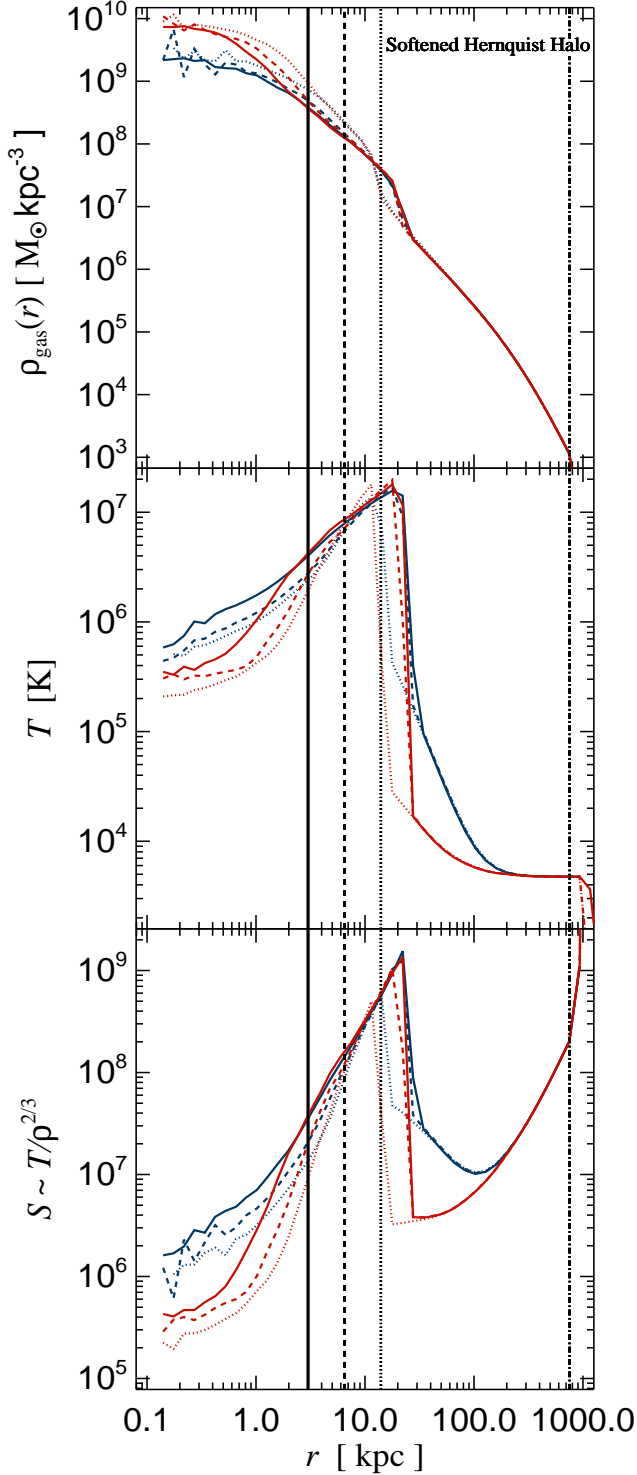


Figure 7. Radial profiles of gas density, temperature and entropy at time $t = 0.1$ Gyr for GADGET (blue lines) and for AREPO (red lines). For each code we show three different resolution runs: $N_{\text{gas}} = 10^4$ and $r_{\text{soft}} = 14.0$ kpc (dotted lines), $N_{\text{gas}} = 10^5$ and $r_{\text{soft}} = 6.5$ kpc (dashed lines) and $N_{\text{gas}} = 10^6$ and $r_{\text{soft}} = 3.0$ kpc (continuous lines). Vertical black lines with the same style indicate the softening scales of the dark matter potential (note that this does not correspond strictly to the spatial resolution limit because the gas is not self-gravitating). The black vertical dot-dashed line denotes the virial radius of the system.

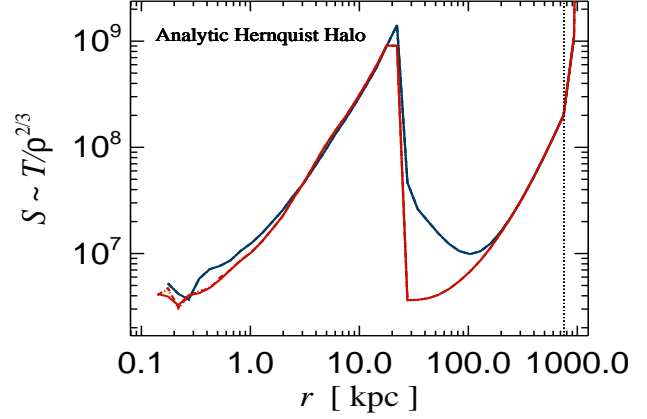


Figure 8. Radial profiles of gas entropy at time $t = 0.1$ Gyr for GADGET (blue lines) and for AREPO (red lines). For each code we show three different resolution runs: $N_{\text{gas}} = 10^4$ (dotted lines), $N_{\text{gas}} = 10^5$ (dashed lines) and $N_{\text{gas}} = 10^6$ (continuous lines), which are largely overlapping. These runs have been computed by adopting an analytic Hernquist dark matter halo without any softening. The black vertical dotted line denotes the virial radius of the system.

both an analytic gravitational potential and a potential with a centrally softened core[†]. We introduce a small modification in the codes such that gas self-gravity is switched off – the gas only feels the static dark matter potential and hydrodynamical forces in a purely non-radiative regime. We then artificially reduce the internal energies of gas particles/cells so as to displace the gas from the equilibrium solution. The newly assigned gas temperature is 4.7×10^3 K, equal for all resolution elements. This test is hence analogous to the well-studied Evrard collapse (Evrard 1988), but it is even simpler in nature because we intentionally neglect gas self-gravity.

As a consequence of the dramatic reduction in its temperature, the gas will suddenly lose pressure support and radially free-fall towards the centre. As the gas collapses, a radial shock develops in the centre, steepening while it propagates outwards and ploughing through the remainder of the outer material which is still falling in. The Mach number of the shock varies over the range $\sim 3 - 8$, well matched to the 1D shock tube test problem described in Section 3.1.1. Finally, as the shock propagates beyond the virial radius of the halo, the gas will reach a new hydrostatic equilibrium solution within the static dark matter potential. In Figure 7, we show radial profiles of gas density, temperature and entropy computed at time $t = 0.1$ Gyr after the start of the gas collapse for dark matter haloes with softened potentials. For each code (GADGET, $N_{\text{gb}} = 64$, $\alpha = 1.0$: blue lines; AREPO: red lines) we perform three runs at different resolutions: $N_{\text{gas}} = 10^4$ and $r_{\text{soft}} = 14.0$ kpc (dotted lines), $N_{\text{gas}} = 10^5$ and $r_{\text{soft}} = 6.5$ kpc (dashed lines) and $N_{\text{gas}} = 10^6$ and $r_{\text{soft}} = 3.0$ kpc (continuous lines). Note that the r_{soft} values indicate the spatial scale over which we smooth the analytic dark matter potential. They do not necessarily rep-

[†] We modify the analytic Hernquist potential by convolving it with the spline softened potential in the centre, as we describe in detail in Section 3.5.

resent the minimum spatial resolution of these simulations, given that the gas is not self-gravitating and that the dark matter halo is rigid. The smoothing lengths of gas particles in the central region are of the order of $r_{\text{hsm1}} \sim 1$ kpc in GADGET for the lowest resolution run with $N_{\text{gas}} = 10^4$, while the typical central cell sizes in AREPO are a few hundred pc.

From Figure 7 it can be seen that there are systematic differences in the gas properties predicted by the simulations with GADGET and AREPO. In particular, the gas entropy distribution is broader in GADGET both in pre- and post-shock gas in all three simulations, while for the two lower resolution runs there is a slight mismatch in the exact position of the shock front and in its strength (similar to the findings for the Evrard collapse in Springel 2010a), which is minimized in the case of $N_{\text{gas}} = 10^6$ particles. Note that the differences in shock front position between different resolution simulations for a given code are not driven by resolution effects but by different spatial softening of the central potential, which affects the gas collapse in the innermost regions. We have checked this explicitly by performing runs with $N_{\text{gas}} = 10^4, 10^5$ and 10^6 for both codes, but this time simulating cold gas collapse within an analytic Hernquist potential, as shown in Figure 8. In this case the shock properties for different resolution runs are almost identical for a given code, indicating that the simulation with $N_{\text{gas}} = 10^4$ resolution elements is in principle sufficient for capturing the shock position accurately. Nonetheless, regardless of the resolution, differences between GADGET and AREPO in the pre- and post-shock gas persist also in the case of analytic Hernquist potentials.

The differences in entropy content of pre- and post-shock gas in GADGET and AREPO are in part due to the large shock broadening in SPH, as discussed in Sections 3.1.1 and 3.1.2. In fact, if we adopt $N_{\text{ngb}} = 32$ (which is considered the minimum number still permissible in three-dimensional simulations) instead of $N_{\text{ngb}} = 64$, the gas entropy profile in GADGET becomes less broad, but is still not as sharp as in AREPO, indicating that simulations with a larger number of particles are needed in GADGET than in AREPO to recover shock features with the same accuracy.

Moreover, there is another numerical effect leading to spatially different entropy generation in GADGET: in the converging subsonic part of the flow, artificial viscosity (as implemented in GADGET) leads to artificial dissipation which increases the entropy in the pre-shock gas. While this feature is clearly visible in Figure 40 of Springel (2010a) for the case of the Evrard collapse, here we see that it also enlarges the central entropy in GADGET. The reason for this is the following: as soon as the gas is brought out of equilibrium and starts free-falling towards the centre, the gas entropy will be boosted in the central region due to an active artificial viscosity in the converging flow, creating an entropy bump that extends up to several kpc (or even several tens of kpc in the case of potentials with large cores) away from the centre, even though the shock has not fully formed yet at this point. This artificial entropy generation is much smaller in AREPO. As the shock forms and propagates outwards, it will lead to additional physical dissipation of much higher magnitude, bringing the entropy profiles of GADGET and AREPO into better agreement. Interestingly, in the case of the Evrard collapse, the initial difference in central entropy profiles is minimized with time due to the

gas self-gravity (as we checked explicitly by running a simulation with exactly the same gas configuration but with gas self-gravity and without static dark matter potential), while it persists in our test runs even when the new equilibrium solution of the system is reached. The central entropy is higher in GADGET by a factor ~ 1.2 and ~ 1.5 for analytic and softened potentials, respectively. Thus it follows that differences in the gas properties due to different spatial dissipation of kinetic energy in GADGET and AREPO can be aggravated in the case of non self-gravitating gas.

Note, however, that the difference in the central entropy profiles between the two codes goes in the opposite direction to what is found in non-radiative simulations of hierarchically forming galaxy clusters, where the central entropy is higher in mesh-based calculations. This indicates that accretion shocks during cosmological structure formation do not seem to be the likely cause of this central entropy discrepancy.

3.3.3 Infall of two gaseous spheres in a static dark matter halo

We now further increase the complexity of the problem by considering two gaseous spheres instead of one, collapsing into one common static dark matter halo placed in-between the two spheres. Each sphere has an initial spatial displacement from the centre of the halo. This test is similar in spirit to a number of previous works which analyzed collisions of two galaxy clusters in isolation (see e.g. Ricker & Sarazin 2001; Ritchie & Thomas 2002; McCarthy et al. 2007; Springel & Farrar 2007; Mitchell et al. 2009; ZuHone 2011), but here we devise a cleaner set-up in order to minimize additional possible numerical effects (e.g. gravitational N-body heating, differences due to gas self-gravity, etc.). As in Section 3.3.2, we simulate a static analytic Hernquist dark matter halo (with exactly the same parameters) but instead of one cold gaseous sphere we generate two identical cold spheres separated by 1.2 Mpc along the x -axis, and we again neglect any radiative losses and gas self-gravity. The gaseous spheres are constructed in the same way as in Section 3.3.2 i.e. gas is first set up to be in hydrostatic equilibrium within a static Hernquist dark matter potential, and then its internal energy is reduced to 4.7×10^3 K. For each code we perform runs with different gas particle numbers, i.e. $N_{\text{gas}} = 10^4$, $N_{\text{gas}} = 10^5$ and $N_{\text{gas}} = 10^6$ per sphere.

Under the gravitational pull from the central dark matter potential the two cold spheres collapse towards its centre and violently collide. The interesting aspect of this problem is that radial symmetry is broken and the gas interaction results in much more complicated shock geometries. This is illustrated in Figure 9, where we show a time sequence of projected gas density maps (first two columns) and mass-weighted entropy maps (last two columns) for runs with $N_{\text{gas}} = 2 \times 10^6$ performed with the two codes. While the GADGET simulation shows qualitatively similar gas structures, the detailed properties substantially differ.

Initially, as the spheres start to fall in, the gas is compressed in the centre of the halo, generating a spherical overdensity, which is somewhat broader and less peaked in GADGET, largely due to a poorer effective spatial resolution and non-negligible artificial viscosity (see Section 3.3.2). Also, during this initial stage more entropy is produced in the

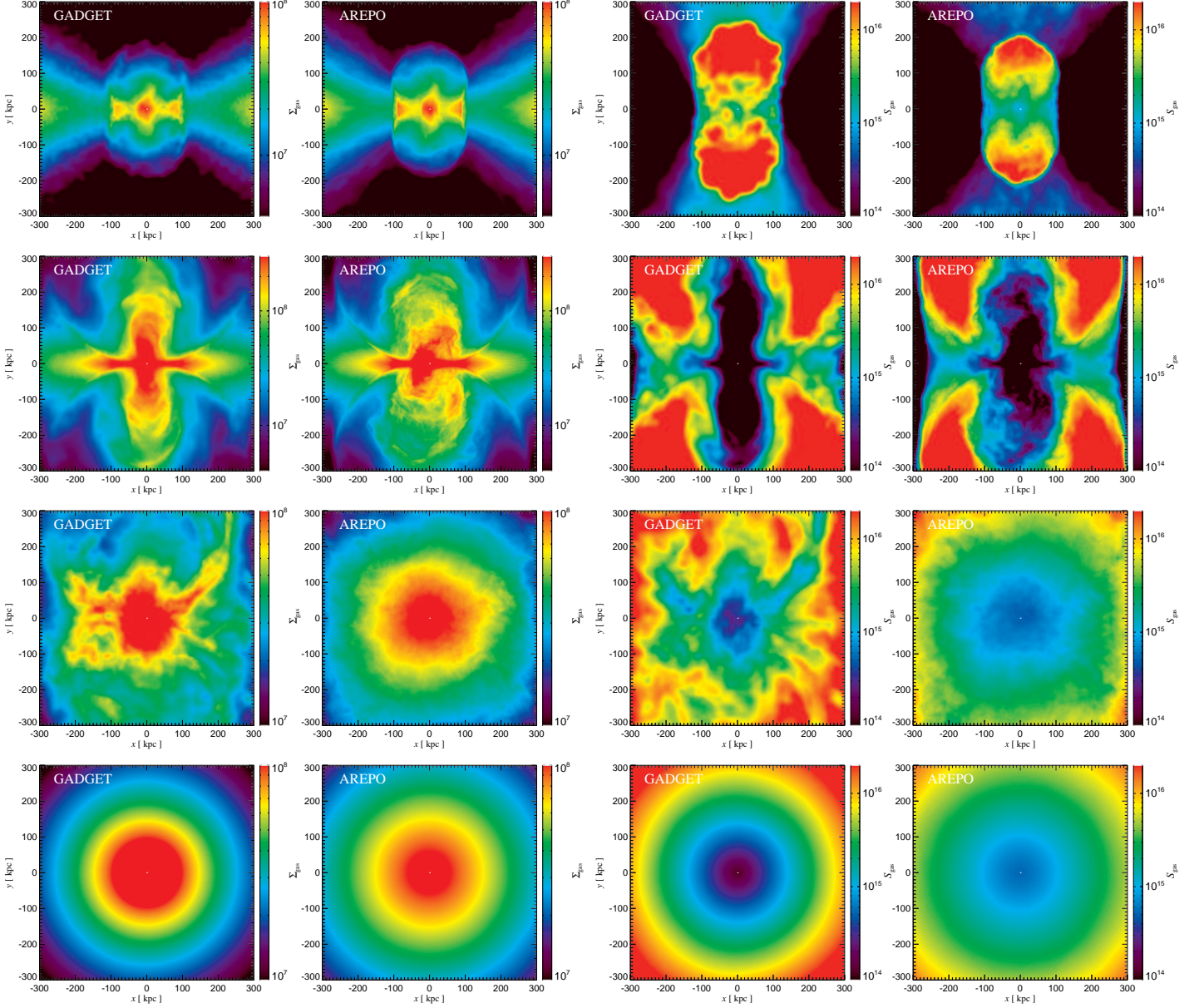


Figure 9. Projected surface density maps (first two columns; in units of $[M_{\odot} \text{kpc}^{-2}]$) and mass-weighted entropy maps (last two columns; in internal units) for GADGET and AREPO simulations, showing the collision of two gaseous spheres with $N_{\text{gas}} = 2 \times 10^6$ at times $t = 0.54$ Gyr (first row), $t = 1.2$ Gyr (second row), $t = 2.9$ Gyr (third row), and $t = 15$ Gyr (fourth row). The plotted spatial domain is $0.6 \times 0.6 \times 1 \text{Mpc}$.

central region in our SPH calculation. As more gas falls in, a shock develops which rapidly assumes a cocoon-like geometry elongated perpendicular to the direction of collapse (see top panels of Figure 9). From the gas density maps it can be seen that the shock front is narrower and sharper in AREPO, whereas in GADGET it has a more splotchy-like appearance, caused by kernel averaging. High entropy plumes propagating outwards along the y -axis are clearly visible in the right-hand panels, where the central entropy in GADGET within $\sim 250 \text{kpc}$ is still higher than in the moving mesh simulation. As the cocoon propagates against the infalling material, gas in the very centre is pushed perpendicular to the x -axis, generating a dense sheet-like region

(see second row of Figure 9). Dynamical fluid instabilities at the boundary of this dense region induce typical mushroom-like morphologies (cap-like in projection). However, even for our highest resolution simulations with $N_{\text{gas}} = 2 \times 10^6$ particles, there are some marked differences between the two codes. Mushroom-like features (corresponding to the red-orange colours in the density maps) originating at the very boundary of the dense central region are more coherent in GADGET, while in AREPO they break up and mix more efficiently with the surrounding medium. This also leads to the more efficient mixing of different entropy gas in the very core in the moving mesh simulation, as can be seen from the entropy maps.

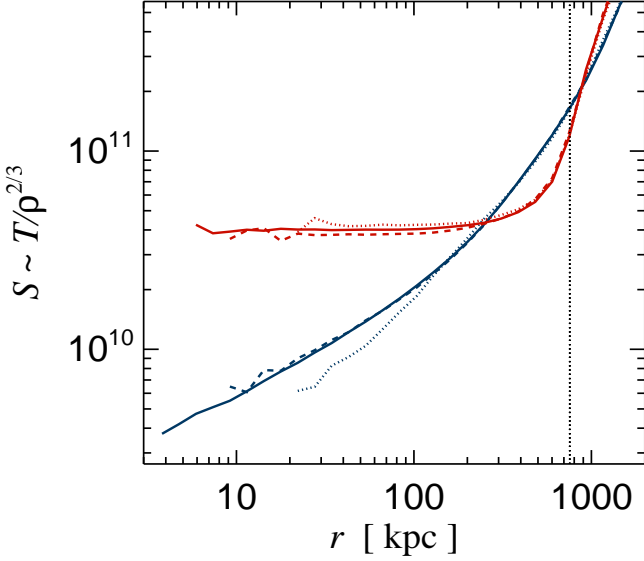


Figure 10. Radial entropy profiles at $t \sim 15$ Gyr from the start of the simulation when the system has reached equilibrium. For each code (GADGET: blue lines; AREPO: red lines) three simulations with increasing gas particle number are shown: $N_{\text{gas}} = 2 \times 10^4$ (dotted lines), $N_{\text{gas}} = 2 \times 10^5$ (dashed lines), $N_{\text{gas}} = 2 \times 10^6$ (continuous lines). The vertical dotted line indicates the virial radius of the underlying dark matter halo. While for $N_{\text{gas}} \geq 2 \times 10^5$ the entropy profiles seem converged for each code, they converge to a very different result.

The differences in the fluid properties at the early stages of the simulated system as described above are, however, not the only reason why the thermodynamic properties of the gas are systematically discrepant between the two codes when a new equilibrium state is reached. With time, dense shells of gas completely disperse by mixing with the surrounding material in AREPO, while in the case of GADGET filaments and blobs of dense gas survive and gradually sink back to the centre (see third row of Figure 9). This buoyantly-driven deposition of low entropy material in GADGET causes even larger differences between the final entropy distributions, which are illustrated in Figure 10 (see also bottom row of Figure 9). The radial entropy profiles are computed once the system has reached hydrostatic equilibrium at time $t \sim 15$ Gyr from the start of the simulation. The blue lines denote GADGET results at three different resolutions (dotted lines: $N_{\text{gas}} = 2 \times 10^4$, dashed lines: $N_{\text{gas}} = 2 \times 10^5$, solid lines: $N_{\text{gas}} = 2 \times 10^6$), while the red lines are for the runs with AREPO. For $N_{\text{gas}} \geq 2 \times 10^5$, both codes seem to produce converged entropy profiles, but they converge to very different results. While in GADGET the entropy profiles steadily decrease towards the centre, in the moving mesh code a large entropy core is produced. This systematic difference in the central entropy profiles is in good agreement with the previous study by Mitchell et al. (2009) of idealized major merger simulations of haloes in the non-radiative regime.

3.3.4 Generalized blob test: non-radiative case

We now devise a numerical experiment to capture the evolution of cold, dense blobs in a more realistic setting, rather than a uniform density windtunnel (see Section 3.2.1). For this purpose we consider our default isolated halo with a static, analytic Hernquist profile for the dark matter component, gas in hydrostatic equilibrium, and we include gas self-gravity, but neglect any radiative losses. We additionally populate this halo with 10 blobs, with the following properties: the gas pressure within blobs is set to be 0.01 of the maximum intracluster pressure within 800 kpc radius from the centre; the radius of each blob is $R_{\text{blob}} = 20$ kpc; the total mass of all blobs is 20% of the total intracluster gas mass, i.e. $M_{\text{blobs}} = 0.2 f_{\text{gas}} M_{\text{halo}}$; the adiabatic index is the same for the blobs and for the surrounding gas, $\gamma = 5/3$.

We place the blobs randomly within a spherical shell with cluster-centric distance of 700 kpc and thickness of 150 kpc, and particles belonging to the blobs are drawn randomly as well. Apart from positions, we also assign bulk velocities to the blobs, while the remainder of the intracluster gas is initially at rest. We set all three components of the velocity vector for each blob, i.e. v_r (only inward radial velocity), v_θ , and v_ϕ , assuming a random distribution for each velocity component starting from a characteristic velocity value of 200 km s^{-1} . Blob velocity values range then from $\sim 230 \text{ km s}^{-1}$ to $\sim 510 \text{ km s}^{-1}$, with the average velocity of all blobs being $v_{\text{mean}} \sim 400 \text{ km s}^{-1}$. In this way, individual blobs will not reach the cluster centre all at the same time, giving them more realistic orbits than purely radial ones. Initially, the blobs are roughly in pressure equilibrium with the surrounding gaseous halo. We perform this numerical experiment at two different resolutions: $N_{\text{gas}} = 10^4$, $N_{\text{blob}} = 10^3$ (low resolution simulation), and $N_{\text{gas}} = 10^5$, $N_{\text{blob}} = 10^4$ (higher resolution simulation).

In Figure 11, we show the time evolution of the dense blobs moving through the isolated halo, for the higher resolution run. In the top panels, the projected surface density map is plotted at the initial time, where both the intracluster gas structure and the blob properties are exactly the same in the two codes. Initially, for $t \leq 1$ Gyr, the blobs are moving on almost identical orbits in GADGET and AREPO, and they also have very similar morphologies. As the blobs start approaching the inner cluster region, well-defined bow shocks develop ahead of each blob and ram-pressure stripping ablates the blobs. Additionally, the Kelvin-Helmholtz and Rayleigh-Taylor instabilities arise which tend to disrupt the blobs on a characteristic timescale of several Gyrs, as discussed in Section 3.2.1 (but note that here gas is self-gravitating). The lower rate of ram pressure stripping and suppression of fluid instabilities in GADGET has a significant effect not only on blob morphologies, but also on their orbits. At $t = 1.37$ Gyr, as illustrated in the middle panels, it is still possible to cross-identify each blob in GADGET with the respective blob in the AREPO run, but the blobs in GADGET have lost less material and thus appear denser and some of them are closer to the centre.

This different loss of blob material leads to systematically diverging orbits due to higher buoyancy and dynamical friction forces acting on each blob in GADGET. This can be clearly seen in the bottom panels where the blobs in GADGET are markedly more concentrated and have es-

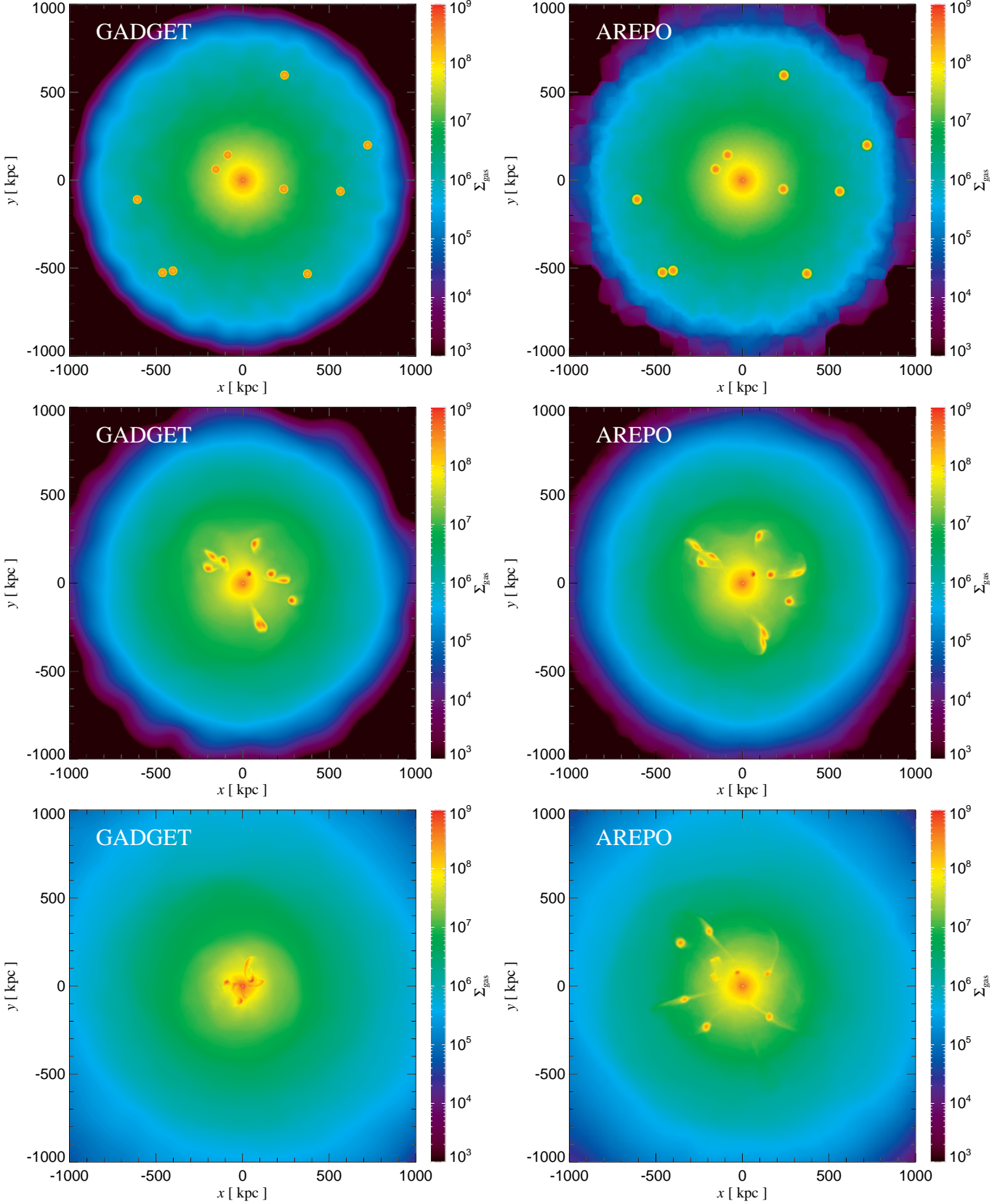


Figure 11. Projected surface density maps in units of $[M_{\odot} \text{kpc}^{-2}]$ at the initial time (top panels), at $t = 1.37$ Gyr (middle panels), and at $t = 2.65$ Gyr (bottom panels) for GADGET ($\alpha = 1.0$, $N_{\text{ngb}} = 64$) and AREPO. The plotted spatial domain is $2 \times 2 \times 2$ Mpc, so as to encompass initially the whole halo whose virial radius is $R_{200} = 755$ kpc. While in the beginning the orbits and the morphologies of the blobs are very similar in the two codes, for $t \geq 1$ Gyr they begin to diverge, with blobs sinking to the centre faster in GADGET.

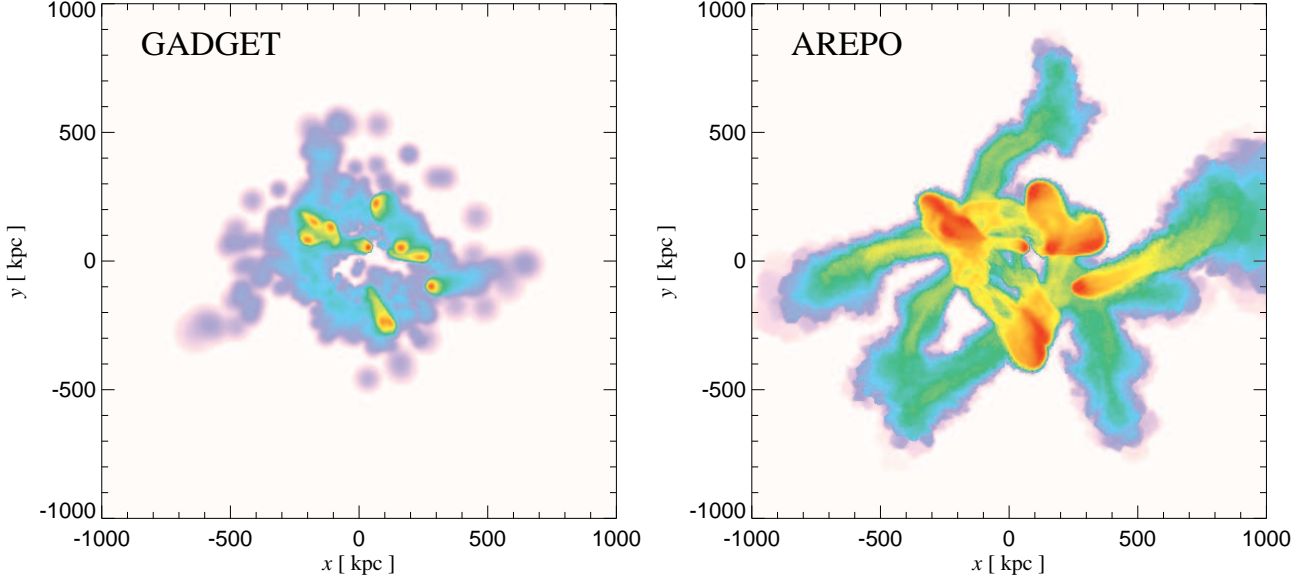


Figure 12. Spatial distribution of gas at $t = 1.37$ Gyr that was contained in the blobs at time $t = 0$. The plotted spatial domain is $2 \times 2 \times 2$ Mpc (for details on map-making see the main text). Most of the material stays confined within blobs in the case of GADGET, with a relatively small fraction lost to their wake. The spatial distribution of blob material is markedly different in AREPO, showing much more stripped gas that creates prominent tails which extend up to several 100 kpc.

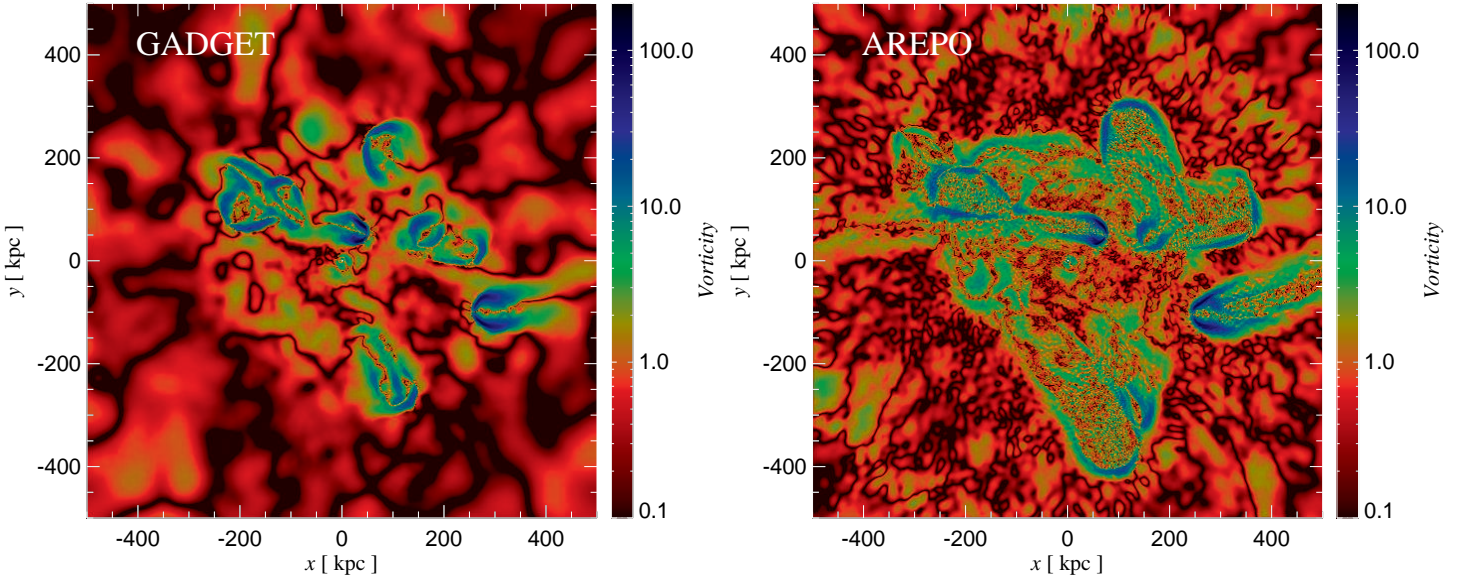


Figure 13. Projected mass-weighted vorticity maps in units of $[\text{km s}^{-1} \text{kpc}^{-1}]$ (absolute value of the z -component only) for a run with GADGET (left-hand panel) and with AREPO (right-hand panel). The maps are computed at time $t = 1.37$ Gyr from the start of the simulation. The thickness of the projected region is $\Delta z = 1$ Mpc. In the wake of the bow shocks produced by the moving blobs turbulence is generated. The spatial extent of the turbulent wakes is significantly larger in AREPO.

essentially all fall to the innermost cluster region, while in AREPO they are at much larger cluster-centric distances being gradually eroded. Moreover, given that the blobs in the moving mesh calculation are ablated more efficiently and that therefore the dynamical friction exerted on the blobs is lower, they have higher velocities when passing at the

pericentre and thus can reach larger distances after the first passage, as visible in the bottom panels of Figure 11. As the gas is self-gravitating, the blobs are also subject to tidal stripping when passing close to the innermost regions which contributes to the ablation of the blob material.

To illustrate more clearly the differences in mass loss of

the blobs in GADGET and AREPO, in Figure 12 we show projected maps of gas material at $t = 1.37$ Gyr (corresponding to the middle panels of Figure 11) which initially belonged to the blobs. To compute these maps in the case of GADGET, we show integrated mass along the line-of-sight ($\Delta z = 2$ Mpc) for all particles initially contained in the blobs. In the case of AREPO, we use a tracer field to follow spreading of fluid elements initially within the blobs: each cell is characterized by an additional scalar field *Tracer* which at $t = 0$ is equal to 1 for all blob cells and 0 elsewhere. The tracer field essentially evolves as a dye cast on the moving fluid, and at some time $t > 0$ the *Tracer* value indicates the mass fraction of the material which initially was in the blobs for each cell. In the right-hand panel of Figure 12, we plot the projected density-weighted tracer field. The dynamical range is the same in both panels, ranging from the maximum of the projected quantity to 10^{-7} of this maximum value, using a logarithmic colour mapping. As anticipated, cold dense blobs in GADGET lose much less material while in the run with AREPO the lost blob material is significantly more diffuse. In the wake of the infalling blobs prominent tails develop, extending up to several 100 kpc. The mass deposition of blob material is clearly much more spatially extended in the moving-mesh code and occurs over larger cluster-centric distances, allowing fluids with different entropies to intermingle and to affect host halo properties on larger scales.

The formation of bow shocks in front of the moving blobs also implies that vorticity will be generated due to the baroclinic term. To explore this issue in more detail, in Figure 13 we show vorticity maps for the run with GADGET (left-hand panel) and for the simulation with AREPO (right-hand panel) at $t = 1.37$ Gyr (corresponding to the middle panels of Figure 11). The vorticity maps are constructed by first evaluating projected mass-weighted velocity maps for the x and y -components, and then by taking the absolute value of the z -component of the curl. Note that while the positions and the structure of the bow shocks are rather similar in the two codes, as expected, there is a striking difference between the spatial extent of the high vorticity regions produced in the wake of the bow shocks (denoted with green colours), where turbulent motions should be generated. For example, focusing on the right-most blob centred on $x \sim 250$ kpc and $y \sim -100$ kpc in projection, the mean projected vorticity value in its wake is a factor of ~ 2 higher in the moving mesh calculation. This clearly suggests that the suppression of vorticity generation in GADGET will have an impact on the level of turbulence injected by curved shocks that are associated with galaxy or subhalo motions through the intracluster medium (ICM), producing a bias in the amount of non-thermal pressure support in galaxy clusters (see also e.g. Dolag et al. 2005; Vazza et al. 2011; Iapichino et al. 2011).

As the blobs orbit at larger cluster-centric distances in AREPO for a longer time and mix with the surrounding medium more efficiently than is the case for GADGET, they lead to higher entropy generation over a wider range of radii. This is shown in Figure 14, where we compute radial entropy profiles for all intracluster gas including the blobs, at the final time $t \sim 10$ Gyr when the system has reached hydrostatic equilibrium. Both in the low and high resolution runs with AREPO the gas entropy profile is significantly higher in the

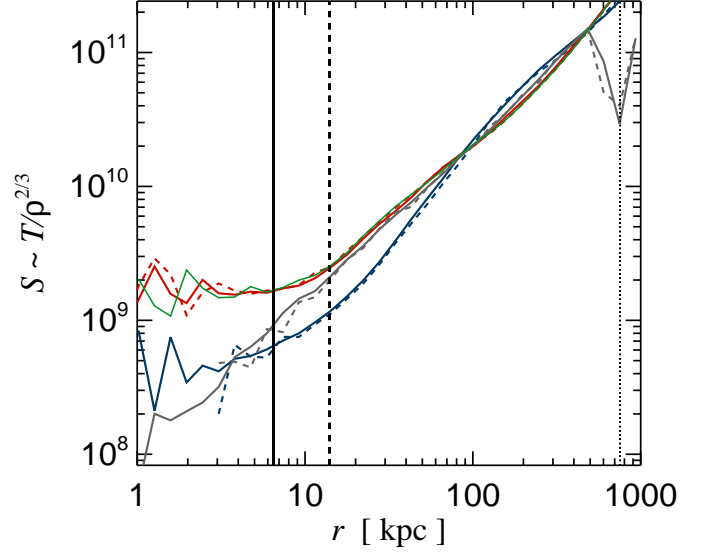


Figure 14. Radial entropy profiles at time $t \sim 10$ Gyr after the start of the simulation, at which point all the blobs have been disrupted and the system has reached a new equilibrium. For each code (GADGET: blue lines; AREPO: red lines) two resolution simulations are shown: $N_{\text{gas}} = 10^4$ and $N_{\text{blob}} = 10^3$ (dashed lines), $N_{\text{gas}} = 10^5$ and $N_{\text{blob}} = 10^4$ (continuous lines). Grey curves with the same line-styles represent the initial entropy profiles of these simulations. Additional green line shows AREPO simulation with $N_{\text{gas}} = 10^4$ and $N_{\text{blob}} = 10^3$, but with the fixed gravitational softening as in GADGET. AREPO runs with adaptive and fixed softenings for the gas produce very similar entropy profiles. Vertical lines with the same line-styles denote the gravitational softenings and vertical dotted line the virial radius of the system. The interaction of the moving dense blobs with the intracluster medium leaves systematically different imprints on the gas entropy profiles when simulated with AREPO or with GADGET.

inner regions up to $r \sim 100$ kpc. Instead, in GADGET, the entropy content of the dense blobs is increased less as they sink towards the centre, such that they settle on a lower adiabat, corresponding to smaller radii. We also note that these systematic differences in entropy profiles are entirely due to the different hydro solvers employed by GADGET and AREPO, and not due to the different choice of gravitational softenings for gas (fixed in GADGET and adaptive in AREPO, but with a floor set equal to the GADGET value). In fact, in Figure 14, the green line shows the entropy profile obtained from an identical low resolution AREPO simulation where instead of an adaptive a constant gravitational softening is used for the gas, in the same way as in GADGET.

It is also instructive to analyze how the entropy profiles of the intracluster medium evolve with time. In Figure 14 we show radial entropy profiles at the initial time (grey lines) for both resolutions. The initial entropy profile of the run with a higher particle number extends further inwards due to the better spatial resolution, while some differences in the outer regions are due to different positions of the blobs which are drawn randomly. The kink in the initial entropy profile for $r \geq 500$ kpc is caused by the blobs which populate this region and have low entropy content with respect to the surrounding ICM. During the first 0.5 Gyr, the en-

entropy profiles in GADGET and AREPO do not change noticeably, remaining nearly identical to each other and to the values prescribed by the initial conditions. At 1 Gyr, the gas entropy starts rising in the very centre in the run with AREPO (it is higher by a factor of ≤ 3 with respect to the initial value), while it takes almost twice as much time in the run with GADGET before the central entropy rises by the same amount. At that time, however, the central entropy profile in AREPO is already about a factor of 6 higher than it was initially, and this systematic difference in the central entropy values persists until the final simulated time.

At time $t \sim 2$ Gyr another interesting process occurs: as several blobs reach the cluster core region for the first time, dissipation of their kinetic energy leads to a gradual expansion of the whole gaseous halo (compare middle to bottom panels of Figure 11) which needs to readjust itself to find a new equilibrium solution within the static dark matter potential.

Interestingly, in a recent paper by Vazza et al. (2011) non-radiative cosmological simulations performed with the GADGET and ENZO codes show that infalling satellites in GADGET sink to smaller radii and are characterized by lower entropy content than is the case for ENZO, confirming the importance of the physical processes discussed here in the full cosmological setting. This indicates that at least part of the systematic difference in central entropy values found between SPH and grid codes in the Santa Barbara cluster comparison project (Frenk et al. 1999) is due to the different treatment of stripping and mixing of the cold material from the infalling satellites.

3.4 Radiative gas cooling in isolated haloes

3.4.1 Radiative gas cooling in non-rotating haloes

We now investigate the time evolution of an isolated $10^{14} M_{\odot}$ mass halo subject to radiative cooling and star formation. We first simulate a halo without any net rotation and compare gas and stellar properties of this system between the two codes. The results illustrated here are for haloes with static dark matter potentials, but we find very similar results if we consider live haloes instead.

In Figure 15 we show star formation rates as a function of time for our simulated object consisting of $N_{\text{gas}} = 10^4$ or $N_{\text{gas}} = 10^6$ particles/cells, calculated either with GADGET or AREPO. Over the whole simulated time-span of 10 Gyr the star formation rates are very similar in the two codes. This indicates that not only do the implemented gas cooling rates match very well, but also that the sub-grid model for star formation and supernova feedback is consistent between the codes, even at a relatively low numerical resolution (a similar conclusion is reached for mergers of isolated galaxies by Hayward et al. 2012).

To demonstrate more clearly that gas radiative cooling and star formation proceed in a very similar manner in our isolated haloes in the absence of any net rotation, in Figure 16 we plot the total mass of cold baryons (stars and gas with entropy $< 10^5$ in internal units) as a function of time for GADGET (blue lines) and AREPO (red lines), at two different resolutions, i.e. $N_{\text{part}} = 10^4$ (dotted lines) and $N_{\text{part}} = 10^6$. For the same number of SPH particles as cells used in AREPO the amount of cold baryons matches to

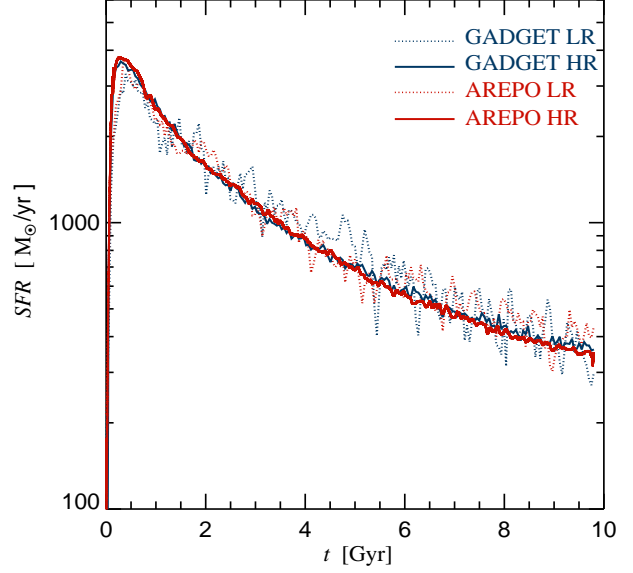


Figure 15. Time evolution of the star formation rate of a $M_{\text{vir}} = 10^{14} M_{\odot}$ isolated halo which radiatively cools and has negligible spin. Illustrated are low ($N_{\text{gas}} = 10^4$; dotted lines) and high ($N_{\text{gas}} = 10^6$; continuous lines) resolution simulations with GADGET (blue) and AREPO (red). The agreement in star formation rates is very good over the whole simulated time-span.

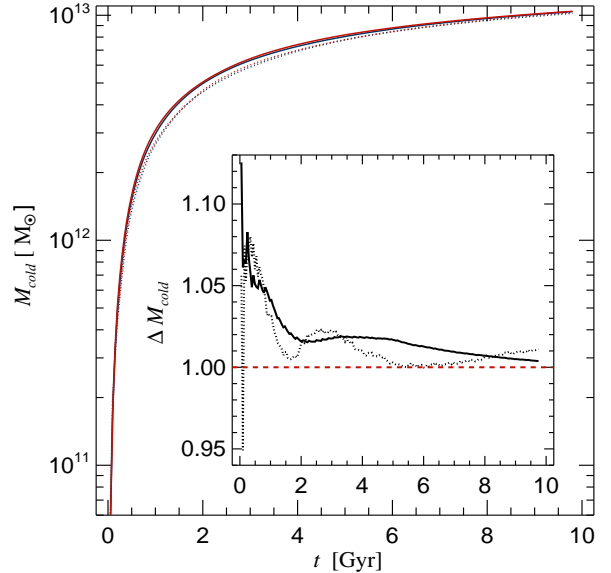


Figure 16. Time evolution of the cold baryonic mass (stars and gas with entropy $< 10^5$ in internal units) for a $M_{\text{vir}} = 10^{14} M_{\odot}$ isolated halo which radiatively cools and has negligible spin. Illustrated are low ($N_{\text{gas}} = 10^4$; dotted lines) and high ($N_{\text{gas}} = 10^6$; continuous lines) resolution simulations with GADGET (blue) and AREPO (red). In the inset, the ratio of M_{cold} values found in AREPO and GADGET is shown for both numerical resolutions. The agreement of the amount of cold baryons formed is extremely good.

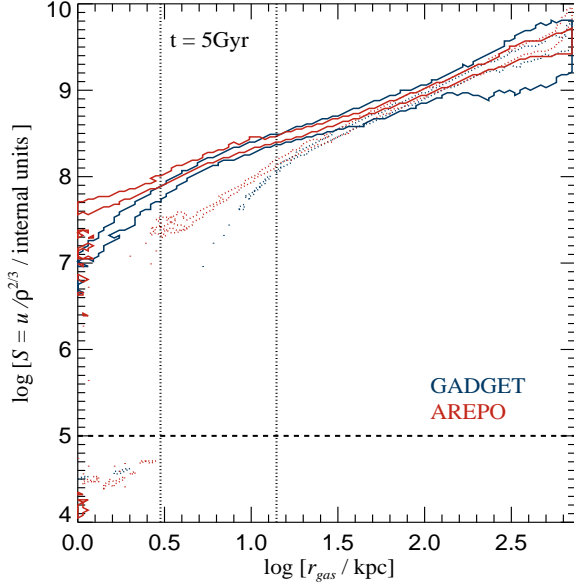


Figure 17. 2D histogram of the gas entropy as a function of radial distance from the centre for GADGET (blue) and AREPO (red) at time $t = 5$ Gyr for $N_{\text{part}} = 10^4$ (dotted lines) and $N_{\text{part}} = 10^6$ (continuous lines). The gaseous halo is allowed to radiatively cool but there is no net rotation. The vertical dotted lines indicate the gravitational softening used in the GADGET run, which correspond to the floor values of the adaptive softening in the moving mesh calculations.

within a few percent between the two codes, as is evident from the inset in the plot where we show the ratio of M_{cold} values found with our moving-mesh code and with GADGET. In the case of live haloes we find that the total mass of cold baryons exhibits the same level of agreement.

Furthermore, in Figure 17 we show a 2D histogram of intracuster gas entropies as a function of cluster-centric distance, after 5 Gyr from the start of the simulation for the low resolution and high resolution runs. The distribution of gas entropies is almost identical in the two codes for $r > r_{\text{soft}}$ (note that below r_{soft} the simulation results are not trustworthy due to the limited gravitational resolution on these scales). It can be seen that there is some difference in the gas entropy close to the virial radius of the system, which is caused by different boundary conditions (vacuum for GADGET and a uniform low resolution grid for AREPO).

These results are in line with the expectation that gas cooling and condensation in this simulated system is determined entirely by the gas properties at the cooling radius (Bertschinger 1989; White & Frenk 1991; Hernquist & Springel 2003) which corresponds very closely between the simulation codes.

3.4.2 Radiative gas cooling in rotating haloes

Even though gas cooling and star formation proceed in a remarkably similar way in GADGET and the moving-mesh code for haloes with vanishing spins, this is not guaranteed to remain the case once some degree of rotation is included. We therefore simulate exactly the same isolated haloes as in the previous section, but imposing a certain level of gas

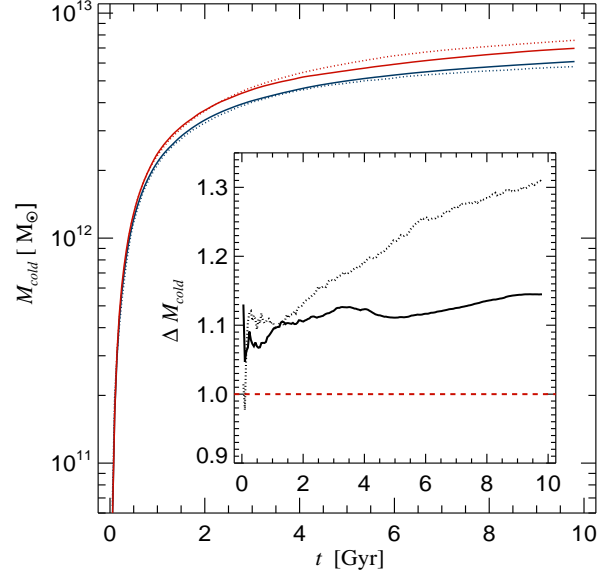


Figure 18. Time evolution of the cold baryonic mass (stars and gas with entropy $< 10^5$ in internal units) for a $M_{\text{vir}} = 10^{14} M_{\odot}$ isolated halo which radiatively cools and has a spin of $\lambda = 0.4$. Illustrated are low ($N_{\text{gas}} = 10^4$; dotted lines) and high ($N_{\text{gas}} = 10^6$; continuous lines) resolution simulations with GADGET (blue) and AREPO (red). In the inset, the ratio of M_{cold} values found in AREPO and GADGET is shown for both numerical resolutions. The agreement between the amount of cold baryons formed is poorer for $N_{\text{gas}} = 10^4$, but improves for the high resolution run, with M_{cold} in AREPO being $\sim 10 - 15\%$ higher.

rotation within the static dark matter potential. To highlight the effect, we use a large spin parameter equal to $\lambda = 0.4$.

Figure 18 shows the time evolution of the total mass in cold baryons (stars and gas with entropy $< 10^5$ in internal units) for the rotating haloes simulated with GADGET (blue curves) and AREPO (red curves) at different resolutions. Comparing M_{cold} with our findings from Figure 16 for non-rotating haloes indicates that overall less gas cools from the hot phase if the gas spins. This effect is not surprising given our initial conditions. Even though the gas density and temperature distribution are initially identical, in the simulations where there is considerable spin the gas will be subject to centrifugal accelerations, preventing it from collapsing radially. The (partial) centrifugal support will tend to reduce the gas densities and hence the cooling rates.

More importantly, from Figure 18 it can be seen that there is poorer agreement in the amount of cold baryons between GADGET and AREPO for a rotating gaseous halo. The discrepancy is larger for the low resolution run with $N_{\text{gas}} = 10^4$, where the final M_{cold} value after 10 Gyr is about 30% higher in the moving-mesh code. The reason for this discrepancy is twofold: at low resolution, GADGET underestimates the cooling rate somewhat, while AREPO overestimates it. The SPH result turns out to be more stable at poor resolution than the mesh-based calculation. Here it is advantageous for SPH that even for few particles a clearly defined phase boundary between cold and hot gas is maintained (in fact, a ‘pressure blip’ in SPH leads to a sampling

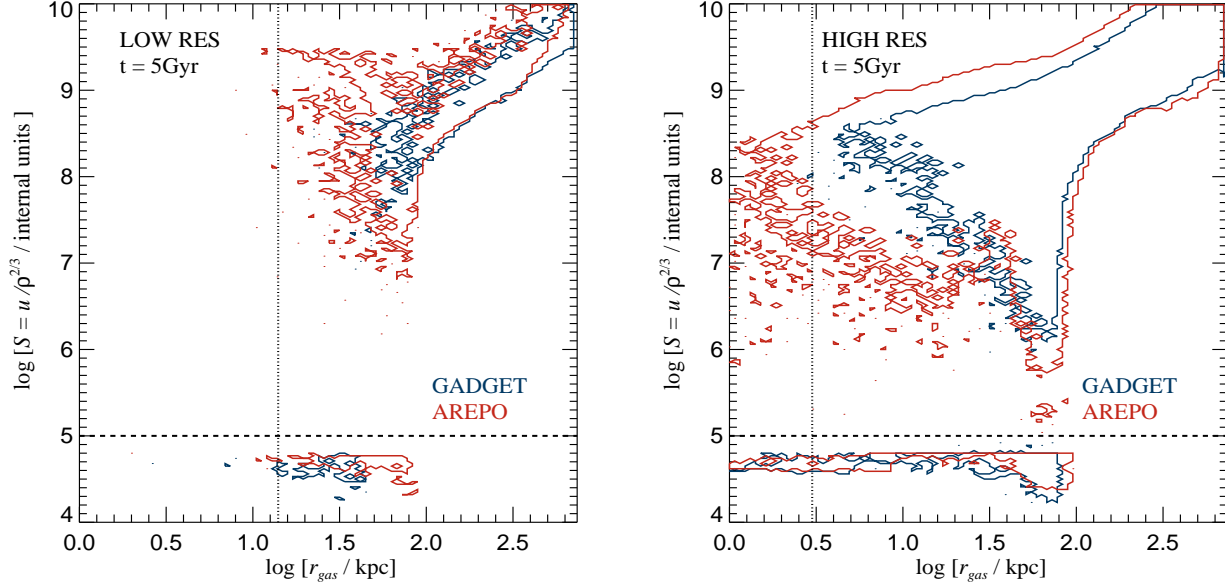


Figure 19. 2D histograms of gas entropy as a function of radial distance from the centre for GADGET and AREPO at $t = 5$ Gyr for the $10^{14} M_{\odot}$ mass halo which radiatively cools and spins at low ($N_{\text{gas}} = 10^4$; left-hand panel) and high ($N_{\text{gas}} = 10^6$; right-hand panel) resolution. The vertical dotted line is the gravitational softening used in the GADGET run, which correspond to the floor value of the adaptive softening in the moving mesh calculations.

gap at this boundary) whereas in AREPO this boundary is blurred at low resolution, causing slightly elevated cooling. This trend is also confirmed by the gas radial velocities which are least negative in the low resolution GADGET run and most negative in the low resolution AREPO simulation. The radial velocities systematically differ within a few 100 kpc and throughout most of the simulated time-span. For $N_{\text{gas}} = 10^6$, the radial velocities obtained with the two codes are much closer, which also translates into a better match of the amount of cold baryons, with M_{cold} higher by $\sim 10 - 15\%$ in AREPO.

At least part of the remaining difference in M_{cold} between GADGET and AREPO is driven by the interaction between the gas which is cooling towards the centre and the cold gas that is already in the disk. This is shown in Figure 19, where we plot 2D histograms of the gas entropy as a function of cluster-centric distance at $t = 5$ Gyr for the low (left-hand panel) and high resolution simulations (right-hand panel). In the moving-mesh code the gas surrounding the central disk has a range of entropy values, with some fluid elements exhibiting very large entropies due to the shock in the immediate vicinity of the disk. Conversely, in the runs with GADGET and especially at low resolution, there is a clear gap between cold material in the disk and hotter gas in the halo (see e.g. Agertz et al. 2007; Springel 2010b). Similarly, as described in Section 3.3.2, SPH particles are affected by artificial viscosity in the converging part of the flow which can slightly offset cooling losses. Note that for $N_{\text{gas}} = 10^6$ the difference in gas entropy structure around the disk is lower between the codes, as expected, given that unwanted artificial viscosity effects are reduced and that the gap between the cold and hot gas phase due to repulsive pressure forces is smaller.

From Figure 19 is it also evident that the extent of the

cold disk is different between the codes, especially at low resolutions. To quantify this important effect, in Table 1 we summarize the main properties of the forming disk. For $N_{\text{gas}} = 10^4$ the half-mass radius of the gaseous disk in GADGET is almost a factor of two smaller than in the higher resolution run, while in the moving mesh code $R_{\text{gas, HM}}$ is 70% of the value we obtain with $N_{\text{gas}} = 10^6$. This indicates that the convergence rate of the gas disk size is slower in the case of GADGET, due to spurious transfer of angular momentum from the cold to the hot phase (Okamoto et al. 2003) and due to the artificial viscosity in the case of poorly resolved disks (note, however, that the total angular momentum is manifestly conserved in GADGET). In the case of the stellar disks they are essentially not resolved in our low resolution runs ($R_{\text{stars, HM}} \sim r_{\text{soft}} = 14$ kpc), while the half-mass radius is $\sim 40\%$ higher in AREPO at higher resolution. Contrary to GADGET, total angular momentum conservation is not automatically guaranteed in the moving mesh code, particularly for disks resolved with only a small number of cells. Nonetheless, it is reassuring that $R_{\text{gas, HM}}$ increases with higher resolution in AREPO (attesting that spurious angular momentum transport inwards is probably small) and that the value of $R_{\text{gas, HM}}$ obtained with both codes for $N_{\text{gas}} = 10^6$ is relatively close. This indicates that the differences in the disk sizes in this numerical experiment are at least partly driven by resolution effects, and in particular by the slow convergence rate of GADGET simulations. Comparing the resolution requirements to obtain good agreement between the codes here with Section 3.4 we note that in the case of cooling gaseous haloes with a significant spin more resolution elements are needed to follow accurately the thermo-dynamical interaction between the central cold disk and the inflowing hotter gas.

code	N_{gas}	$R_{\text{gas,max}}$ [kpc]	$R_{\text{gas,HM}}$ [kpc]	$M_{\text{gas,HM}}$ [$10^{10} M_{\odot}$]	$R_{\text{stars,HM}}$ [kpc]	$M_{\text{stars,HM}}$ [$10^{10} M_{\odot}$]	M_{cold} [$10^{10} M_{\odot}$]
GADGET	10^4	40.0	30.3	27.0	13.5	215.3	484.6
GADGET	10^6	79.0	54.7	9.8	6.8	238.3	496.2
AREPO	10^4	79.0	47.4	27.7	18.1	267.9	591.2
AREPO	10^6	85.0	67.1	12.8	9.7	263.1	551.8

Table 1. Gaseous and stellar properties of the disk at $t = 5$ Gyr which forms in an isolated $10^{14} M_{\odot}$ halo which radiatively cools and rotates. For simulations with two different resolutions with GADGET and AREPO, we list the maximum radial extent of the gaseous disk, its half-mass radius and the total mass within the half-mass radius, in the third, fourth and fifth columns, respectively. Stellar half-mass radius and the total stellar mass enclosed within it are shown in the sixth and seventh columns. In the eighth column the total mass of cold baryons is given, being equal to $2 \times (M_{\text{gas,HM}} + M_{\text{stars,HM}})$. All gas particles/cells with entropy less than 10^5 (in internal units) are assumed to be part of the disk, while for the stellar disk we consider all star particles that form in the simulated volume.

code	N_{gas}	N_{blob}	$R_{\text{gas,max}}$ [kpc]	$R_{\text{gas,HM}}$ [kpc]	$M_{\text{gas,HM}}$ [$10^{10} M_{\odot}$]	$R_{\text{stars,HM}}$ [kpc]	$M_{\text{stars,HM}}$ [$10^{10} M_{\odot}$]	M_{cold} [$10^{10} M_{\odot}$]
GADGET	10^4	10^2	22.0	16.3	12.9	13.5	184.4	394.8
GADGET	10^5	10^3	45.0	17.9	7.5	15.8	221.1	457.1
GADGET.EOS	10^5	10^3	24.0	7.6	154.4	/	/	308.9
GADGET	10^6	10^4	56.0	32.9	5.4	26.6	235.1	481.0
AREPO	10^4	10^2	76.0	37.8	16.8	17.8	199.9	433.5
AREPO	10^5	10^3	71.0	43.0	17.3	21.8	261.3	557.2
AREPO.EOS	10^5	10^3	76.0	13.4	244.7	/	/	489.5
AREPO	10^6	10^4	75.0	41.5	12.7	32.7	273.2	571.9

Table 2. Gaseous and stellar properties of the disk at $t = 5$ Gyr that formed in an isolated $10^{14} M_{\odot}$ halo which radiatively cools, rotates and contains 10 orbiting substructures. For simulations with three different resolutions with GADGET and AREPO we list the maximum radial extent of the gaseous disk, its half-mass radius and the total mass within the half-mass radius, in the fourth, fifth and sixth columns, respectively. Stellar half-mass radius and the total stellar mass enclosed within it are shown in the seventh and eighth columns. In the ninth column the total mass of cold baryons is given, being equal to $2 \times (M_{\text{gas,HM}} + M_{\text{stars,HM}})$. All gas particles/cells with entropy less than 10^5 (in internal units) and within $R_{\text{gas,max}}$ are assumed to be part of the disk, while for the stellar disk we consider all star particles that form in the simulated volume (including the blobs). We also list the gaseous disk properties in two additional simulations, denoted by EOS, performed at intermediate resolution. In these simulations we adopt the standard sub-grid model for star formation, with the dense, cold gas lying on the effective equation-of-state, but we prevent any spawning of star particles.

3.4.3 Generalized blob test: radiative case

Here we consider the evolution of cold, dense blobs embedded in a galaxy cluster as in Section 3.3.4, but now the whole system is allowed to radiatively cool. To add an additional layer of realism the blobs are constructed to be similar to cosmological substructures: they are equipped with their own dark matter halo, and stars may form out of their gas during the simulated time-span. More specifically, each blob is represented by a live Hernquist dark matter halo and gas in hydrostatic equilibrium. The virial mass of each blob is $2 \times 10^{12} M_{\odot}$, the scale length parameter is $a = 41.4$ kpc, and the gas fraction amounts to $f_{\text{gas}} = 0.17$. As before, we populate our default $10^{14} M_{\odot}$ halo (that has a static dark matter potential) with 10 identical substructures. The procedure for assigning blob positions and velocities is the same as in Section 3.3.4, but here we use a different random number seed which leads to the different initial positions and velocities with respect to Section 3.3.4. The positions of blob centres are in the range of ~ 650 to ~ 750 kpc, while the characteristic blob velocities range from 200 to 500 km s^{-1} . Also, in Section 3.3.4 the gas in the halo is initially at rest while here the gas has considerable angular momentum, which contributes to the relative velocity between the blobs and

the gas. We simulate the evolution of this system at three different resolutions: $N_{\text{gas}} = 10^4$, $N_{\text{blob}} = 10^2$ (low resolution), $N_{\text{gas}} = 10^5$, $N_{\text{blob}} = 10^3$ (intermediate resolution), and $N_{\text{gas}} = 10^6$, $N_{\text{blob}} = 10^4$ (high resolution), with gas self-gravity, and with cooling and the sub-grid model for star formation.

Additionally, we perform two simulations at intermediate resolution where the standard sub-grid model for star formation is included as well, but where we simply prevent any star particles from being spawned out of the star-forming phase, denoted by EOS. This simulation set-up is particularly useful for following the thermodynamical evolution of cold and hot gas for many Gyrs without the dense cold gas being subject to fragmentation that would likely occur in pure cooling runs. For numerical experiments with AREPO, as a default choice, we have not used mesh refinement and de-refinement. However, we have performed extra runs at intermediate resolution where we adopt a de-/refinement strategy to limit the mass range of gas cells (within a factor of 2 of the gas particle mass in the matching GADGET run) which automatically imposes a narrow range of stellar masses as well. For these runs we have increased the number of gas cells/particles in each blob to 2.5×10^3 , such that the gas particle/cell mass in blobs is exactly iden-

tical to the one in the parent halo (which is optimal for our de-/refinement method). These test runs recover very closely all of our results with the default set-up, confirming that N-body heating effects (e.g. due to the spectrum of star particle masses) are not very important here.

In Figure 20, we show projected surface density maps at $t = 0.9$ Gyr, $t = 2.3$ Gyr, and $t = 6$ Gyr for simulations where we use the sub-grid model for star formation, but prevent the spawning of star particles. Initially the evolution of the blobs proceeds in a very similar fashion in simulations with GADGET and AREPO. However, already after less than a Gyr (see top panels of Figure 20) blobs in the moving mesh code are much more affected by ram pressure and dynamical fluid instabilities, which cause efficient gas stripping. As the blobs reach the very inner regions, they interact with the forming disk. In GADGET simulations, the blobs have a significantly more damaging effect on the disk, simply because they are less gas depleted. This is clearly visible in the central panels of Figure 20, where in GADGET feeble spiral features are present, while in AREPO the disk is more extended and spiral arms are well developed. Additionally, in the moving-mesh simulation a large fraction of the stripped material is deposited in the main halo, and is gradually accreted onto the central disk, promoting its growth. Blobs in GADGET are more coherent and eventually lose their angular momentum due to hydro-/dynamical friction. As they merge with the central disk, an ellipsoidal structure is formed (see bottom panels of Figure 20). Note that due to the static dark matter halo the dynamical friction force arises only due to the gas in the main halo. Thus, we expect the blobs will lose their angular momentum on an even faster time-scale in simulations with live dark matter haloes, as is the case for cosmological runs. After 6 Gyrs, the difference between GADGET and AREPO simulations is significant: while in the latter case an extended disk forms, with gaseous spiral arms reaching up to 60 kpc away from the centre, in GADGET we are left with a flattened, amorphous blob.

In numerical experiments where we do not suppress star particles from forming, we find very similar results. In Figure 21, we show projected stellar density maps at $t = 6$ Gyr using our intermediate resolution simulations (which both in resolution and in time match the bottom panels of Figure 20). Clearly, the stellar distribution in GADGET is more centrally concentrated, forming a small disk. On the contrary, a well-defined extended stellar disk assembles in the moving-mesh calculation, endowed with a central bar. We quantify the properties of gaseous and stellar disk in Table 2. The convergence rate of the gas disk size in GADGET is even slower than in the simulations without blobs, because additionally to the spurious transfer of the angular momentum the damaging effect of the blobs is the highest in the low resolution runs, where gas stripping is largely suppressed. This leads to larger systematic difference in disk sizes between the two codes with resolution, but for the highest resolution runs AREPO disks are only about $\sim 30\%$ larger.

The interaction of cold blobs with the surrounding medium influences the global star formation rates as well. In Figure 22, we compare the star formation histories in simulations without blobs (left-hand panel; see Section 3.4.2) with the numerical tests where haloes are populated with 10 sub-structures (right-hand panel). In the case without blobs, the star formation rates are somewhat higher in AREPO espe-

cially for the low resolution run due to the more efficient gas cooling and thus larger amounts of cold gas available for star formation. For the high resolution run the differences in star formation rates between the codes are smaller, given that difference in the amount of cold gas between the codes amount to $\sim 30\%$. The difference in the star formation rates between the codes becomes more pronounced once we include the blobs. Initially, as can be seen from the inset plot where we show the star formation rate from the blobs and from the disk separately, the star formation rate within blobs contributes more than 50% to the total star formation rate, and it is very similar in both codes. This induces a much higher peak in the total star formation rate in the right-hand panel with respect to the simulations without blobs. For $t > 1$ Gyr the star formation rate in the AREPO blobs dramatically drops, and at ~ 2 Gyr it is truncated altogether. This is due to ram-pressure stripping and dynamical fluid instabilities that efficiently remove the gas from the blobs. In fact, we can crudely estimate a characteristic Kelvin-Helmholtz timescale at the initial time using the equation from Section 3.2.1 (but note that here gas is self-gravitating), where for the blob density we take the average density within the blob radius R_{blob} (which we varied from the scale length parameter to the virial radius) and for the surrounding medium density we take the typical halo density at the position of the blobs. With these assumptions we obtain typical values for t_{KH} in the range of 1 – 3 Gyr, depending on the blob positions, relative velocities and the choice of R_{blob} . These t_{KH} values are comparable to the timescale on which star formation within the blobs is suppressed in AREPO. In GADGET simulations, star formation proceeds in the blobs even until 9 Gyrs, albeit at a progressively reduced rate. For $t > 1$ Gyr the total star formation rate comes mainly from the central regions. The central disks that form in the AREPO simulations have higher star formation rates over many Gyrs, which are typically larger by a factor of 2 than the GADGET results. Even in our highest resolution moving mesh simulation the star forming disk has roughly twice as large amount of cold gas, a difference which originates from the interaction of hotter infalling gas with the gas in the disk, as described in Section 3.4.2. However, also the star-forming gas is distributed over a larger area. In fact, while within the half-mass radius of the GADGET disk the star formation rate is $\sim 40\%$ higher in the moving mesh run, outside of it is a factor ~ 2.3 higher, contributing about half to the total AREPO star formation rate. The reason why cold, star forming gas in GADGET is filling a smaller area in the disk and is more confined to the dense arm segments and blobs (the so called “string-of-pears”, which can be also seen in the middle panel of Figure 20), is due to the SPH surface tension originating at the interface between cold and hot media in relative motion. In the right-hand panel of Figure 22 we also show an identical intermediate resolution AREPO run, but with fixed gas gravitational softening, the same as in the matching GADGET run. It can be seen that the choice of gas gravitational softening in AREPO does not affect our results in any significant way: both the evolution of the SFR in the central disk and in the orbiting blobs remains very similar, indicating that the differences that we see between the two codes are indeed entirely driven by hydrodynamical effects.

These findings have immediate consequences for more

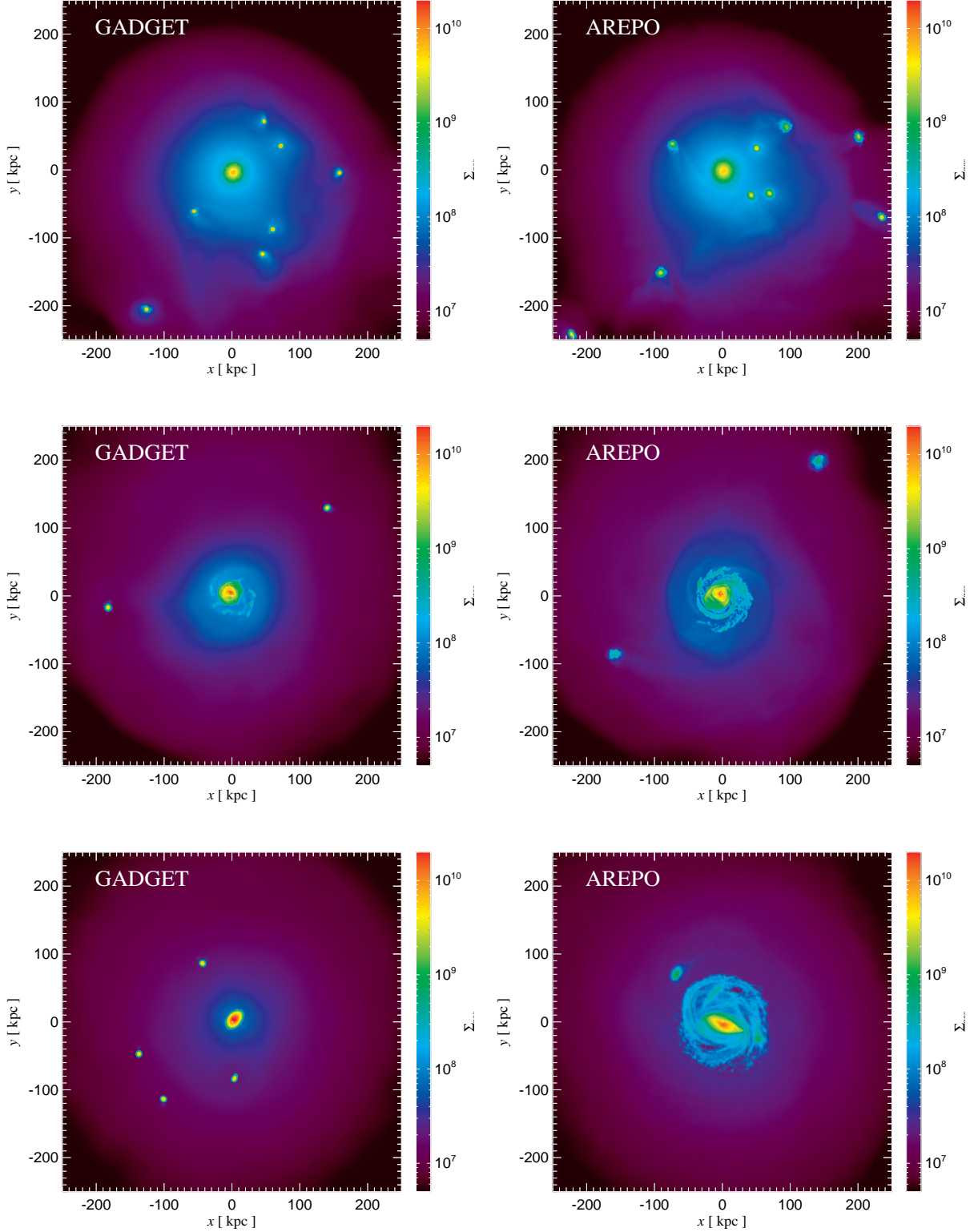


Figure 20. Projected surface density maps in units of $[M_{\odot} \text{kpc}^{-2}]$ at times $t = 0.9 \text{ Gyr}$ (top panels), $t = 2.3 \text{ Gyr}$ (central panels), and $t = 6 \text{ Gyr}$ (bottom panels) for a $M_{\text{vir}} = 10^{14} M_{\odot}$ isolated halo which rotates, radiatively cools, and has 10 orbiting substructures. The thickness of the projection is $\Delta z = 2 \text{ Mpc}$. Although we have used our sub-grid model for star formation in these simulations, spawning of star particles has been intentionally prevented here. Gas stripping from the orbiting blobs is found to be very different in the two numerical techniques. In GADGET, blobs largely survive, and when they interact with the central disk they tend to disrupt it, whereas in AREPO, the blobs are more easily shredded and have a less damaging effect on the forming disk. In fact, some of the stripped blob material ends up contributing to the extended gaseous disk.

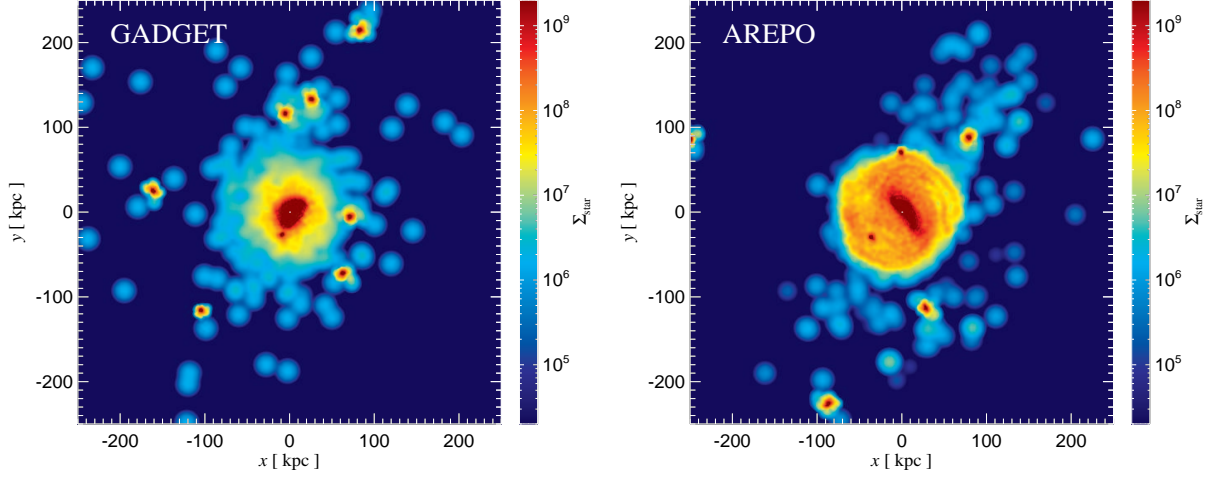


Figure 21. Projected stellar density maps in units of $[M_{\odot} \text{kpc}^{-2}]$ at $t = 6 \text{ Gyr}$ for a $M_{\text{vir}} = 10^{14} M_{\odot}$ isolated halo which rotates, radiatively cools, forms stars, and has 10 orbiting substructures. The maps have been constructed from our intermediate resolution runs and the thickness of the projection is $\Delta z = 2 \text{ Mpc}$. While in GADGET a centrally concentrated disk forms that is surrounded by a feeble thick structure, in the simulation with AREPO, a well-defined extended stellar disk assembles with a central bar.

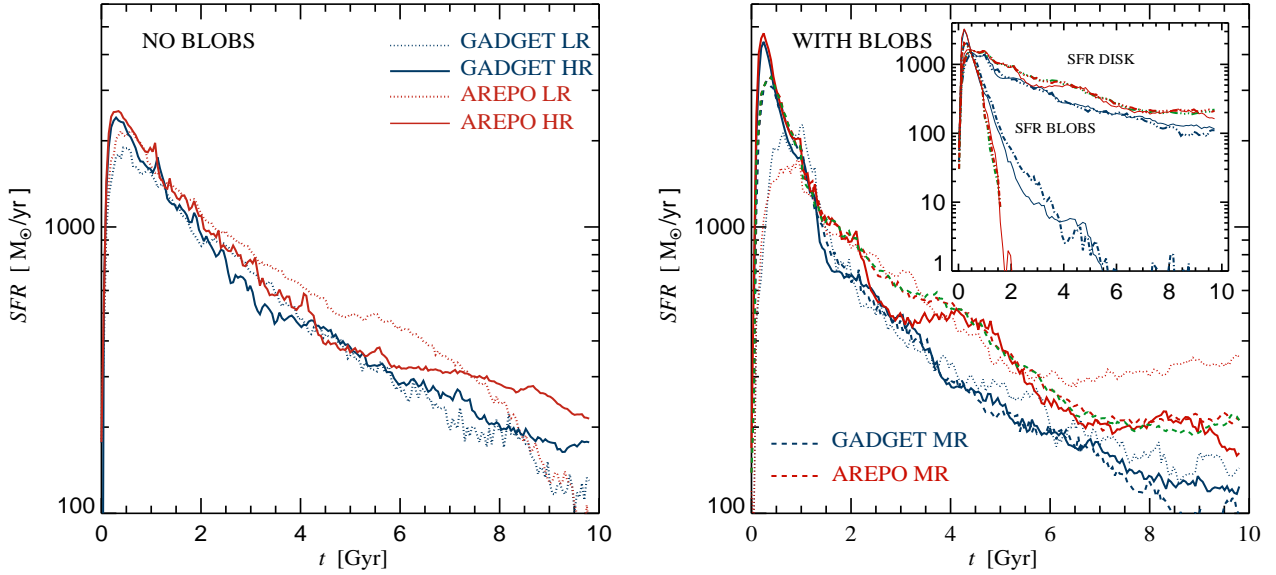


Figure 22. Time evolution of the star formation rate of a $M_{\text{vir}} = 10^{14} M_{\odot}$ isolated halo which radiatively cools and rotates. In the left-hand panel we show simulations without blobs, while in the right-hand panel the haloes contain 10 orbiting substructures. In the right-hand panel, the curves give results from simulations with three different resolutions, with GADGET and AREPO, using $N_{\text{gas}} = 10^4$ (LR), $N_{\text{gas}} = 10^5$ (MR), and $N_{\text{gas}} = 10^6$ (HR) particles/cells. In the left-hand panel, only low and high resolution simulations are shown. In the simulations without blobs, the star formation rates are somewhat higher in AREPO, but the relative difference increases when we include the blobs. Higher star formation rates in AREPO emanate from the central disk which contains a greater amount of cold, star-forming gas which fills a larger area. In the inset plot, we compute the total star formation rate occurring within the blobs (dot-dashed and continuous lines) and the one coming from the disk (triple dot-dashed and continuous lines) for our intermediate and high resolution simulations with GADGET (blue curves) and AREPO (red curves). In the right-hand panel we also show intermediate resolution AREPO run with the fixed gravitational softening for the gas (green lines) which produces very similar SFRs (both in the disk and in the blobs) as the simulation with the adaptive softening.

realistic astrophysical situations. For example, Puchwein et al. (2010) have simulated a high-resolution sample of galaxy clusters with GADGET finding that up to 30% of intracluster stars form in dense cold blobs – remnants of infalling satellites. Suppressed dynamical instabilities in GADGET enhance the probability of survival for these dense blobs, which can then serve as sites of star formation, thus possibly over-predicting the number of intracluster stars. In fact, if we compute the total mass of cold baryons M_{cold} (stars plus gas above the density threshold for star formation) in two cosmological simulations (for further details see Paper I) where in one we prevent the spawning of stars and in the other we allow it (the simulations are otherwise identical), M_{cold} is found to be very similar in GADGET regardless of whether stars are formed or not. Instead, in the simulations with AREPO, we find that M_{cold} is systematically reduced at lower redshifts if the spawning of stars is prevented. This demonstrates explicitly that very low entropy material formed in GADGET cannot easily be shredded and mixed with higher entropy gas (at least in the absence of additional feedback processes such as galactic winds or black hole heating), so that M_{cold} is preserved (a similar conclusion has been reached independently by Heß & Springel 2011). In contrast, in the simulations with AREPO if star formation is switched-off some of the cold material can be stripped out of galaxies due to dynamical instabilities, returning it to diffuse form and lowering M_{cold} . Importantly, this also implies that the number of stars formed in AREPO will be much more sensitive to the characteristic timescale for star formation and to the numerical resolution (needed to resolve fluid instabilities) than is the case for GADGET. In a recent paper by Agertz et al. (2011) it has been shown that lower star formation efficiency leads to the production of larger disks in cosmological simulations. While this result is in line with our findings, it is important to recognize that the actual cause is quite different: in the study by Agertz et al. (2011), differences in the physical modelling of star formation in cosmological simulations affect the disk sizes, while here the cause lies in different accuracies of the hydro solvers involved.

3.5 Gravitational N-body heating

We now investigate potential artificial gas heating due to the Poisson noise induced by the finite number of particles in dark matter haloes. Steinmetz & White (1997) outlined the analytic theory of this effect, and confirmed it with non-radiative and radiative numerical experiments that quantified gravitational N-body noise present in structure formation simulations. For an equilibrium system they defined a characteristic N-body heating timescale which is proportional to the cube power of the dark matter velocity dispersion and inversely proportional to the dark matter particle mass and dark matter density. Due to this inverse proportionality to the dark matter density, N-body heating is expected to be strongest in the innermost regions of haloes. From their analysis it follows that the dark matter particle mass adopted in numerical simulations should be lower than a critical mass which is of order of few times $10^9 M_{\odot}$ for galaxy clusters (see their equation [10]), otherwise the radiative cooling losses may be overwhelmed by spurious heating.

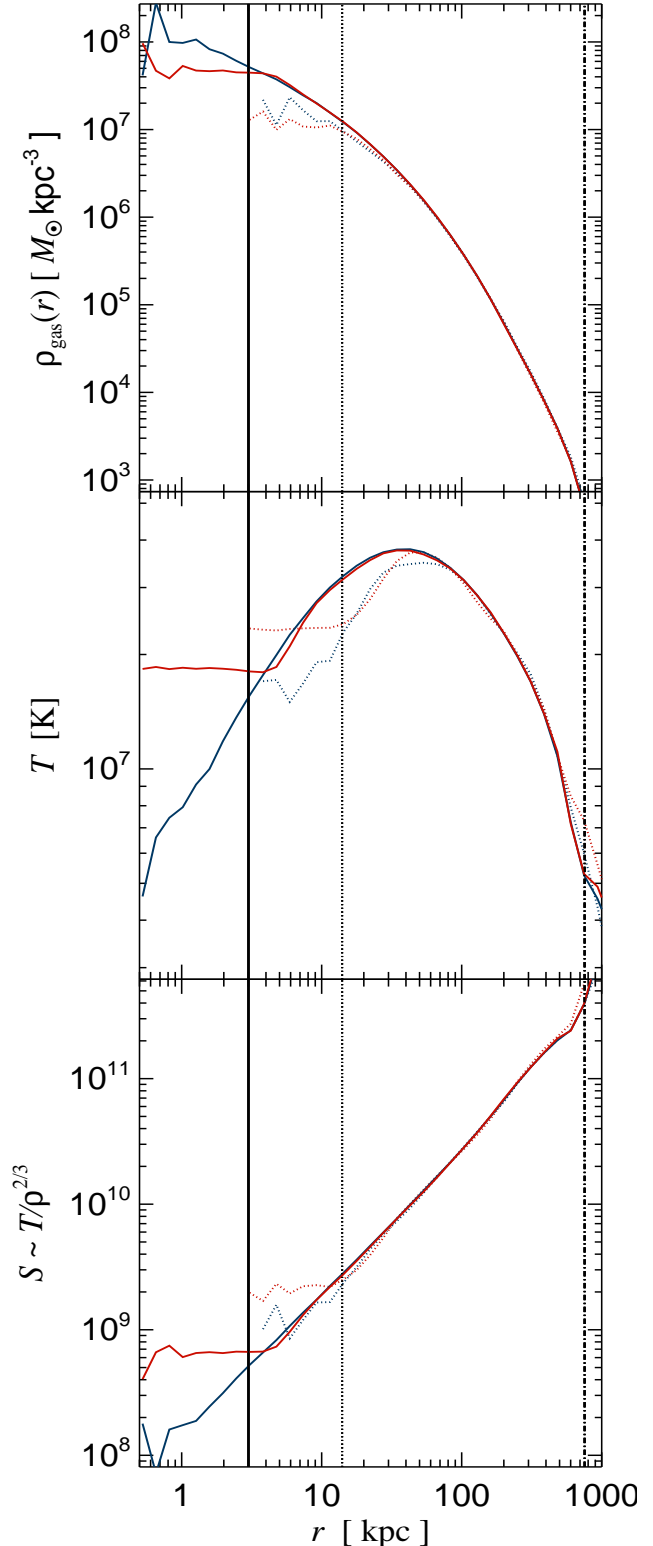


Figure 23. Radial profiles of gas density, temperature and entropy at time $t \sim 10$ Gyr for GADGET (blue lines) and for AREPO (red lines). For each code we show two different resolution runs: $N_{\text{gas}} = 10^4$ and $r_{\text{soft}} = 14.0$ kpc (dotted lines), and $N_{\text{gas}} = 10^6$ and $r_{\text{soft}} = 3.0$ kpc (continuous lines). The vertical black lines with the same style indicate the softening scale of the dark matter potential, whereas vertical dot-dashed lines show the virial radius of the system.

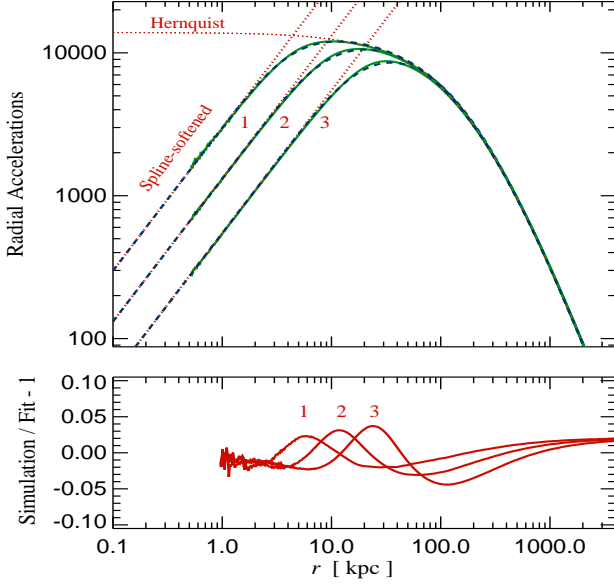


Figure 24. Comparison of fitting functions for spline-softened gravitational accelerations (equation 4; blue dashed lines) with actual gravitational accelerations obtained from very high resolution runs with matching r_{soft} values (green continuous lines). The limiting cases of spline-softened accelerations for small and large radii are illustrated with dotted red lines. The bottom panel shows the residuals of our fitting functions over the relevant range of radii.

Since nowadays the typical mass resolution of hydrodynamical cosmological simulations has improved dramatically, with simulated galaxy clusters containing several times 10^6 up to 10^7 particles in zoom-in runs (Dolag et al. 2009; Sijacki et al. 2009; Vazza et al. 2010), possible numerical artifacts due to a grainy dark matter distribution are rarely addressed in the literature (but see e.g. Kay et al. 2000; Borgani et al. 2006; Vazza 2011). Recently, Springel (2010a) has pointed out that mesh based codes are potentially more severely affected by gravitational N-body heating than SPH codes, due to their better ability to detect weak shocks, which in this case is an unwanted feature.

Here we perform a number of idealized test problems aimed at explicitly addressing the N-body heating problem, and in particular to understand whether there are systematic differences between GADGET and AREPO in this respect. Note that intentionally all previous tests (except for Section 3.4.3) have been performed either without any dark matter component or with a static dark matter potential to avoid such possible Poisson-noise imprints.

We first consider our standard isolated halo, where we replace the static dark matter potential with a live dark matter halo in which dark matter particles have a characteristic velocity dispersion for the given mass of the system (but there is no net rotation). As in the case of the rigid potential, we populate the halo with gas particles in hydrostatic equilibrium which are initially at rest. We include self-gravity of the gas component and evolve the system non-radiatively for 10 Gyr.

In Figure 23, we show radial profiles of gas density, temperature and entropy at the final time for both codes at two resolutions: $N_{\text{gas}} = N_{\text{DM}} = 10^4$ particles (dotted lines)

and $N_{\text{gas}} = N_{\text{DM}} = 10^6$ particles (continuous lines). The centre of the system is defined by the position of the most bound particle. For cluster-centric distances greater than the gravitational softening value, r_{soft} , the entropy profiles of GADGET and AREPO agree to within $\sim 20\%$ for the low resolution runs, and to better than 10% for the high resolution simulation. For $r < r_{\text{soft}}$, the differences between the codes in the entropy profile amount up to a factor of 2, with the gas entropy in AREPO being systematically higher. An extra test simulation performed with AREPO in its dual entropy mode (where entropy instead of energy is explicitly conserved for cells whose Riemann problems with adjacent cells all have Mach number less than 1.1) resulted in identical radial profiles as for the AREPO simulation in the standard energy mode. This clearly indicates that the small entropy core which develops in AREPO is not caused by weak shocks generated by the grainy dark matter potential. Rather, central gas particles/cells acquire small scale velocities when simulated with live haloes. In the case of the moving-mesh code, these velocities lead to fluid mixing and temperature equilibration in the innermost regions, while in GADGET such mixing does not occur. Note, however, that in the gravitating systems, r_{soft} represents the minimum spatial scale below which the simulation results are not trustworthy due to discreteness effects. Therefore, provided that gravitational softening lengths are chosen conservatively, the gas properties of galaxy clusters in an equilibrium configuration simulated with GADGET and AREPO match very well.

We now consider a more challenging problem, where we simulate the infall of cold gas into dark matter haloes. This is the same problem discussed in Section 3.3.2, but here we compare outcomes from live versus static dark matter haloes. To match numerical experiments with rigid and live haloes as closely as possible we adopt the following procedure.

For live haloes, the motion of dark matter particles is prevented in the code to avoid local deformations of the gravitational potential which will not be present in the static case. Effectively, in this way the distribution of dark matter is “frozen”, and live haloes are coarse grained representations of static haloes.

For static haloes, we convolve the analytic Hernquist potential with a spline softened potential in the centre, such that gas particles feel exactly the same gravitational acceleration as in the case of live haloes, where the central potential needs to be softened to minimize effects from two-body encounters. For the Hernquist potential, gravitational accelerations are given by

$$g(r) = -\frac{GM_{\text{vir}}}{(r+a)^2}. \quad (3)$$

We modify the gravitational acceleration felt by gas particles in the code, viz.

$$g(r) = -\frac{GM_{\text{vir}}}{\left(\frac{32\pi r}{3h_0^3 M_{\text{vir}}}\right)^{-1} + (r+a)^2 \exp(-h_1/r)}, \quad (4)$$

where h_0 and h_1 are free coefficients (to first approximation $h_0 \sim h_1 \sim r_{\text{soft}}$). We determine the value of h_0 and h_1 for three different resolution runs by fitting equation (4) to the gravitational acceleration of a live “frozen” halo with 10^7 dark matter particles simulated three times assuming r_{soft}

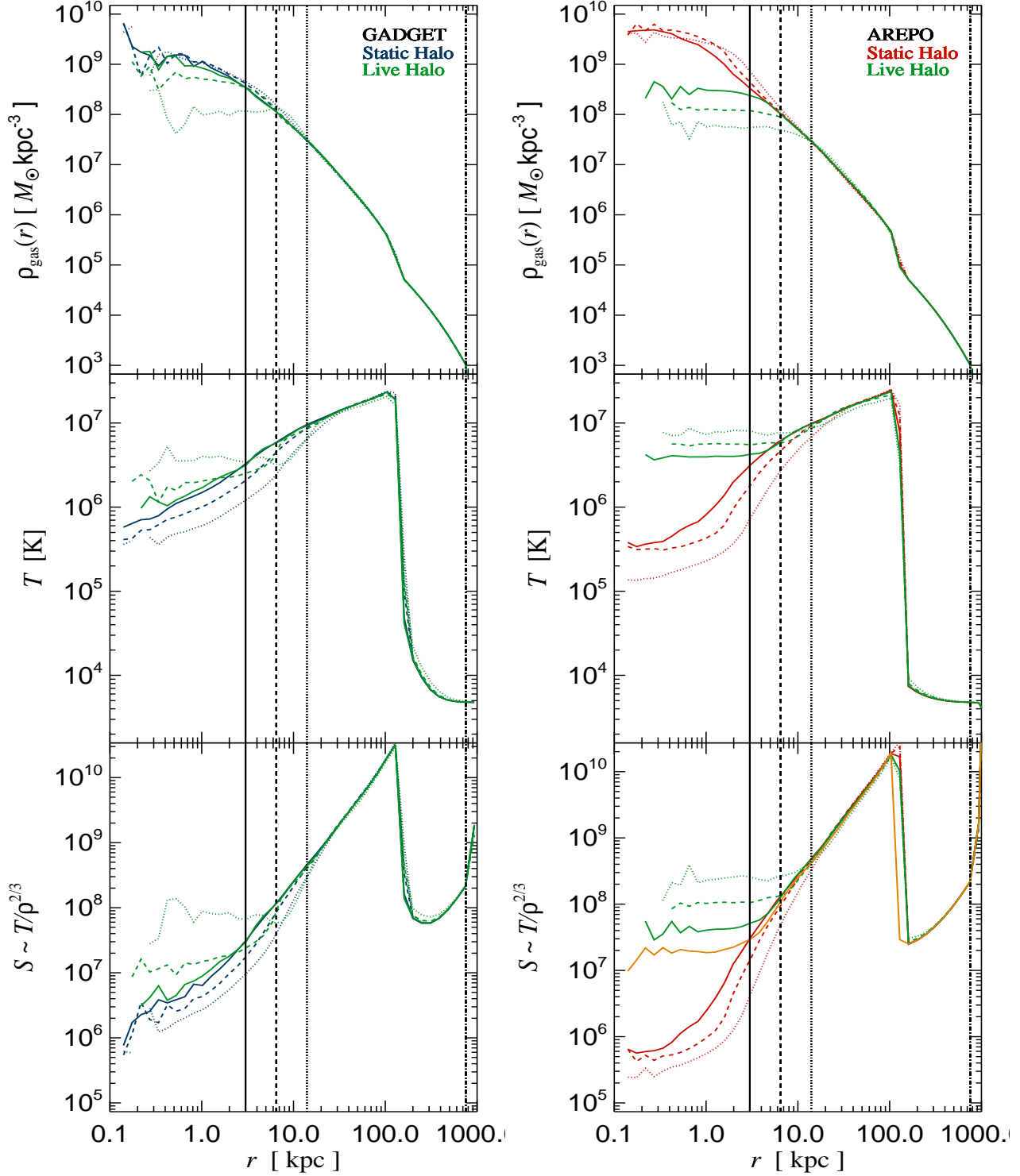


Figure 25. Radial profiles of gas density, temperature and entropy at time $t = 0.3$ Gyr for GADGET (left-hand panels; blue lines: static dark matter haloes; green lines: live dark matter haloes) and for AREPO (right-hand panels; red lines: static dark matter haloes; green lines: live dark matter haloes). For each code we show three different resolution runs: $N_{\text{DM}} = 10^4$ and $r_{\text{soft}} = 14.0$ kpc (dotted lines), $N_{\text{DM}} = 10^5$ and $r_{\text{soft}} = 6.5$ kpc (dashed lines) and $N_{\text{DM}} = 10^6$ and $r_{\text{soft}} = 3.0$ kpc (continuous lines), while $N_{\text{gas}} = 10^6$ is kept fixed. In the right-hand panel we also show the entropy profile obtained with the moving-mesh code in the entropy mode for our highest resolution simulation (continuous orange line). The vertical black lines with the same style indicate the softening scales of the dark matter potential. The black vertical dot-dashed lines denote the virial radius of the system.

values appropriate for the numerical resolutions we want to investigate.

In Figure 24 we illustrate the outcome of this method. In the upper panel, the green lines denote the radial gravitational acceleration of the live “frozen” halo with 10^7 dark matter particles, adopting $r_{\text{soft}} = 3, 6.5$ and 14 kpc (indicated by numbers 1, 2 and 3), respectively. Blue dashed lines are our best fit functions to these simulations using equation (4). Dotted red lines indicate the radial acceleration in the case of the analytic Hernquist profile and of the spline-softened potential, which are the limiting cases of equation (4) for large and small radii, respectively. The bottom panel of Figure 24 shows how accurate our modified gravitational acceleration is as a function of cluster-centric distance.

With the procedure described above we perform simulations of radial infall of cold gas into live (“frozen”) haloes. We keep the number of gas resolution elements the same and equal to $N_{\text{gas}} = 10^6$ (corresponding to $r_{\text{soft,gas}} = 3$ kpc for GADGET, while gravitational softenings are adaptive in AREPO but with a floor of 3 kpc), while we increase the number of dark matter particles from $N_{\text{DM}} = 10^4$ ($r_{\text{soft,DM}} = 14$ kpc), to 10^5 ($r_{\text{soft,DM}} = 6.5$ kpc) and 10^6 ($r_{\text{soft,DM}} = 3$ kpc). For each live halo we run a matching static halo simulation where the number of gas particles/cells is kept the same, i.e. $N_{\text{gas}} = 10^6$. In all runs, gas self-gravity is neglected and there are no radiative losses. In close encounters of gas and dark matter, the effective gravitational softening is the maximum between $r_{\text{soft,gas}}$ and $r_{\text{soft,DM}}$, such that $r_{\text{soft,DM}}$ is the relevant length scale of the problem.

In Figure 25 we show radial profiles of gas density, temperature and entropy at time $t = 0.3$ Gyr (analogous to Figure 7). The left-hand panels are for simulations of live and static haloes with GADGET, while the right-hand panels show the results with AREPO. Due to gravitational N-body heating there are systematic differences in the central gas properties. The central gas density is lower, while the central gas temperature and entropy are higher for the live haloes, due to spurious transfer of energy from dark matter to gas, which heats the gas and makes it expand. In general, N-body heating effects are largest for $N_{\text{DM}} = 10^4$ and smallest for $N_{\text{DM}} = 10^6$, and they are confined to spatial regions within $r_{\text{soft,DM}}$, which is reassuring. We can see by comparing the left-hand to the right-hand panels that AREPO is indeed much more sensitive to spurious gravitational heating, as discussed in Springel (2010a), with the central entropy boosted by two orders of magnitude. In the right-hand panel of Figure 25, we also show radial entropy profile obtained with AREPO in the dual entropy mode (where entropy instead of energy is explicitly conserved for cells with all Mach numbers less than 1.1) with $N_{\text{DM}} = 10^6$ particles (orange continuous line). This indicates that at least part of the central entropy core is generated by the weak shocks which gas cells experience when moving through the grainy dark matter potential.

At the final time $t = 2.45$ Gyr, when the system has reached an equilibrium state, the difference between the matching live and static halo runs for $r > r_{\text{soft,DM}}$ is $\sim 10\%$, $\sim 5\%$, and $\sim 5\%$, respectively, for low, intermediate and high resolution in GADGET, while it is somewhat higher in AREPO, i.e. $\sim 15 - 20\%$, 10% , and 5% , respectively. For

$r < r_{\text{soft}}$ the ratios of central entropy values are ≤ 10 , ≤ 4 and ≤ 2 in GADGET and ≤ 300 , ≤ 150 and ≤ 25 in AREPO, for low, intermediate and high resolution runs. Even though the amount of artificial heating is significantly larger in AREPO than it is for GADGET, the departures between static and live halo radial profiles always occur within $r_{\text{soft,DM}}$ for both codes. Provided that gravitational softening values for the dark matter component are chosen cautiously, our numerical experiments hence indicate that the systematic discrepancy in central entropy values found between SPH and mesh-based codes for the Santa Barbara cluster comparison project (Frenk et al. 1999; Springel 2010a) is unlikely to be due to effects from a grainy dark matter potential during cosmological structure formation.

4 DISCUSSION AND CONCLUSIONS

In this study we have carried out a detailed comparison between the SPH code GADGET and the new moving-mesh code AREPO on a number of hydrodynamical test problems, which are crucial for understanding cosmological simulations of galaxy formation. In a purely hydrodynamical regime without gas self-gravity or an external gravitational potential we have first carried out a set of numerical experiments previously considered in the literature, some of which have rarely been shown for SPH codes, such as the 2D implosion test. We have then focused on idealized non-radiative galaxy cluster simulations, specifically aimed towards benchmarking differences in hydro solvers for problems with shocks and fluid instabilities. In simulations where radiative losses were included we have analyzed the amount of baryons which cool from the hot halo atmospheres in GADGET and AREPO, both for rotating and non-rotating haloes. In the former case, we have also studied how the central baryonic disks form, and how orbiting substructures affect the disk morphology and the star formation rate. Finally, we have constructed special test problems designed to gauge the effect of gravitational N-body heating on the gaseous properties of the haloes. Our main conclusions are as follows:

- While post-shock fluid properties are captured well both in GADGET and AREPO in the case of 1D shock tube tests with high Mach numbers, the shocks are significantly broader in GADGET, and substantial post-shock oscillations develop, largely because of an inadequate treatment of the initial contact discontinuity. AREPO in the moving-mesh mode preserves the contact discontinuity much more accurately, but it is broadened if we employ a static mesh, due to larger numerical diffusivity in this case. Note that the more accurate treatment of the contact discontinuity in the moving mesh code can lead to a larger ‘wall heating’ effect (Rider 2000) than in static grid codes, which tend to wash-out at some level the initial start-up errors at the contact discontinuity (see also description of the Noh problem in Springel 2010a).

- For shocks with complicated geometries in multi-dimensions, differences between GADGET and AREPO are more striking. Even though the global fluid properties remain similar, the sampling of the fluid properties is much noisier in GADGET, and the development of dynamical fluid instabilities is inhibited. These problems are not specific to GADGET, but are inherent to the standard SPH method as

a whole (see also Agertz et al. 2007; Springel 2010b, and discussion in Section 2.1.2). The suppression of fluid instabilities reduces the amount of entropy generation by mixing and artificially prolongs the lifetime of gaseous structures which are moving through a medium with a different density. Additionally, vorticity generation in the wake of curved shocks due to the baroclinic source term is largely suppressed in GADGET, which directly impacts angular momentum transfer by vortices and the level of generated turbulence.

- These fundamental differences between GADGET and AREPO identified in simple hydrodynamical test problems affect the properties of gas in more realistic, cosmologically motivated simulations as well. Specifically, in non-radiative idealized simulations of merging galaxy clusters and in simulations of isolated haloes with orbiting gaseous substructures we find that in AREPO: *i*) an entropy core is produced in the centre due to more efficient fluid mixing, *ii*) the gas stripping rate from the orbiting substructures is larger, and *iii*) more vorticity is produced in the wake of curved shocks. These findings are in line with results of previous works which simulated similar problems with AMR codes (e.g. Mitchell et al. 2009; Vazza et al. 2011; Vazza 2011). Moreover, unphysical dissipation of shocks and subsonic turbulence in GADGET, as shown by Bauer & Springel (2012) (see also Section 4.2 of Paper I), leads to the heating of the halo outskirts rather than of the central regions.

- In radiative simulations of isolated haloes without any net rotation, gas cooling and condensation into stars proceeds in a very similar fashion in GADGET and AREPO, given that the gas properties at the cooling radius match closely. However, for spinning haloes there is a net difference in the total amount of cold baryons, which is higher in AREPO, and this difference persists at a level of about 10 – 15% in our highest resolution runs. Baryonic disks which form due to dissipative collapse of rotating gas are systematically larger in AREPO at low resolution, and the convergence rate of the gas disk sizes is higher.

- In numerical experiments where we follow the interaction between a forming central disk and 10 orbiting substructures in an isolated halo which radiatively cools, the final disk morphology is significantly different. While in AREPO an extended disk is produced with well developed spiral arms and a central bar, in GADGET the disk is more centrally concentrated and amorphous. Orbiting substructures are much more efficiently stripped of their gas content in the moving-mesh calculation and the material is incorporated into the host halo atmosphere. Instead, in GADGET gaseous substructures are more coherent, thus they lose more angular momentum from hydro-/dynamical friction, and when passing through the central disk they induce morphological transformations.

- While star formation is more readily truncated in infalling substructures due to gas stripping, extended gaseous disks in AREPO have significantly larger star formation rates for many Gyrs than is the case for GADGET.

- Due to its better ability to detect weak shocks, AREPO is more sensitive to gravitational N-body heating (Springel 2010a). This is confirmed by our specifically designed numerical experiments, which allow us to quantify the magnitude of spurious gas heating for simulations of haloes with a finite number of dark matter particles with respect to the analytic dark matter potentials. Nonetheless, the spatial ex-

tent of this artificial heating is reassuringly constrained to lie within the gravitational softening length for typical setups, which is a scale below which simulation results are not trustworthy due to resolution effects anyway.

The numerical experiments presented in this study clearly demonstrate that several important shortcomings of the SPH solver not only affect idealized test problems but are equally detrimental in more realistic setups relevant for structure formation, and ultimately in full cosmological simulations. This is especially the case because of: *i*) the complicated flows involving multiphase media which are the norm in cosmological simulations, and *ii*) the hierarchical nature of structure formation where low mass systems are always poorly resolved. In both of these regimes the hydrodynamical solver of the standard SPH method exhibits the largest inaccuracies. On the other hand, our numerical tests confirm and significantly extend the findings of Springel (2010a) that the moving-mesh code AREPO delivers a physically more accurate representation of the evolution of inviscid gases. Note that in the current work we deliberately kept the modelling of the baryon physics at a very simple level, so as to isolate the differences between the hydro solvers in as clean a manner as possible. While inclusion of more realistic feedback mechanisms, such as supernovae winds and AGN heating, will likely modify the properties of the simulated galaxies significantly, it is of prime importance to disentangle numerical inaccuracies of the hydro solver from the uncertainties of the feedback physics modelling. It is hence clear that cosmological simulations with AREPO have the potential to provide a much more realistic description of structure formation in the Universe (see also Papers I and II), something we will explore in more depth in forthcoming studies.

ACKNOWLEDGEMENTS

We would like to thank Andrew MacFadyen and Daniel Eisenstein for very useful discussions and suggestions on the topic, and Manfred Kitzbichler and Diego Muñoz for carefully reading the manuscript. We would like to thank the anonymous referee for many constructive suggestions, which helped to improve the presentation of the results. DS acknowledges NASA Hubble Fellowship through grant HST-HF-51282.01-A. DK acknowledges NASA Hubble Fellowship through grant HST-HF-51276.01-A. The computations in this paper were performed on the Odyssey cluster supported by the FAS Science Division Research Computing Group at Harvard University.

REFERENCES

- Abel T., 2011, *MNRAS*, 413, 271
- Agertz O., Moore B., Stadel J., Potter D., Miniati F., Read J., Mayer L., Gawryszczak A., Kravtsov A., Nordlund Å., Pearce F., Quilis V., Rudd D., Springel V., Stone J., Tasker E., Teyssier R., Wadsley J., Walder R., 2007, *MNRAS*, 380, 963
- Agertz O., Teyssier R., Moore B., 2011, *MNRAS*, 410, 1391
- Balsara D. S., 1995, *Journal of Computational Physics*, 121, 357
- Barnes J., Hut P., 1986, *Nature*, 324, 446

- Bauer A., Springel V., 2012, MNRAS, p. 3102
- Bertschinger E., 1989, ApJ, 340, 666
- Borgani S., Dolag K., Murante G., Cheng L.-M., Springel V., Diaferio A., Moscardini L., Tormen G., Tornatore L., Tozzi P., 2006, MNRAS, 367, 1641
- Cha S.-H., Whitworth A. P., 2003, MNRAS, 340, 73
- Crain R. A., Theuns T., Dalla Vecchia C., Eke V. R., Frenk C. S., Jenkins A., Kay S. T., Peacock J. A., Pearce F. R., Schaye J., Springel V., Thomas P. A., White S. D. M., Wiersma R. P. C., 2009, MNRAS, 399, 1773
- De Villiers J.-P., Hawley J. F., 2003, ApJ, 589, 458
- Di Matteo T., Khandai N., DeGraf C., Feng Y., Croft R. A. C., Lopez J., Springel V., 2012, ApJ, 745, L29
- Dolag K., Borgani S., Murante G., Springel V., 2009, MNRAS, 399, 497
- Dolag K., Vazza F., Brunetti G., Tormen G., 2005, MNRAS, 364, 753
- Evrard A. E., 1988, MNRAS, 235, 911
- Frenk C. S., White S. D. M., Bode P., Bond J. R., Bryan G. L., Cen R., Couchman H. M. P., Evrard A. E. e. a., 1999, ApJ, 525, 554
- Gammie C. F., McKinney J. C., Tóth G., 2003, ApJ, 589, 444
- Hayward C., et al., 2012, in preparation
- Heitmann K., Lukić Z., Fasel P., Habib S., Warren M. S., White M., Ahrens J., Ankeny L., Armstrong R., O'Shea B., Ricker P. M., Springel V., Stadel J., Trac H., 2008, Computational Science and Discovery, 1, 015003
- Hernquist L., 1987, ApJS, 64, 715
- Hernquist L., 1990, ApJ, 356, 359
- Hernquist L., Katz N., 1989, ApJS, 70, 419
- Hernquist L., Springel V., 2003, MNRAS, 341, 1253
- Heß S., Springel 2011, MNRAS, submitted
- Heß S., Springel V., 2010, MNRAS, 406, 2289
- Hui W. H., Li P. Y., Li Z. W., 1999, Journal of Computational Physics, 153, 596
- Iapichino L., Schmidt W., Niemeyer J. C., Merklein J., 2011, MNRAS, 414, 2297
- Inutsuka S.-I., 2002, Journal of Computational Physics, 179, 238
- Janka H.-T., Langanke K., Marek A., Martínez-Pinedo G., Müller B., 2007, Phys. Rep., 442, 38
- Katz N., Weinberg D. H., Hernquist L., 1996, ApJS, 105, 19
- Kay S. T., Pearce F. R., Jenkins A., Frenk C. S., White S. D. M., Thomas P. A., Couchman H. M. P., 2000, MNRAS, 316, 374
- Keres D., et al., 2011, MNRAS, submitted, astro-ph: 1109.4638
- Klessen R. S., Krumholz M. R., Heitsch F., 2009, Special Issue on Computational Astrophysics, Eds. Lucio Mayer, Advanced Science Letters, 4, 258-285 (2011)
- Marri S., White S. D. M., 2003, MNRAS, 345, 561
- McCarthy I. G., Bower R. G., Balogh M. L., Voit G. M., Pearce F. R., Theuns T., Babul A., Lacey C. G., Frenk C. S., 2007, MNRAS, 376, 497
- Mitchell N. L., McCarthy I. G., Bower R. G., Theuns T., Crain R. A., 2009, MNRAS, 395, 180
- Morris J. P., Monaghan J. J., 1997, Journal of Computational Physics, 136, 41
- Murante G., Borgani S., Brunino R., Cha S.-H., 2011, MNRAS, accepted, astro-ph: 1105.1344
- Okamoto T., Jenkins A., Eke V. R., Quilis V., Frenk C. S., 2003, MNRAS, 345, 429
- O'Shea B. W., Nagamine K., Springel V., Hernquist L., Norman M. L., 2005, ApJS, 160, 1
- Pretorius F., 2007, "Relativistic Objects in Compact Binaries: From Birth to Coalescence", Editor: Colpi et al., Publisher: Springer Verlag, Canopus Publishing Limited, eprint arXiv:0710.1338
- Price D. J., 2008, Journal of Computational Physics, 2271, 10040
- Puchwein E., Springel V., Sijacki D., Dolag K., 2010, MNRAS, 406, 936
- Rasio F. A., 2000, Progress of Theoretical Physics Supplement, 138, 609
- Read J. I., Hayfield T., Agertz O., 2010, MNRAS, 405, 1513
- Ricker P. M., Sarazin C. L., 2001, ApJ, 561, 621
- Rider W. J., 2000, Journal of Computational Physics, 162, 395
- Ritchie B. W., Thomas P. A., 2001, MNRAS, 323, 743
- Ritchie B. W., Thomas P. A., 2002, MNRAS, 329, 675
- Robinson M., Monaghan J. J., 2011, arXiv:1101.2240
- Saitoh T. R., Makino J., 2012, ApJ submitted, arXiv: 1202.4277
- Sijacki D., Springel V., Haehnelt M. G., 2009, MNRAS, 400, 100
- Springel V., 2005, MNRAS, 364, 1105
- Springel V., 2010a, MNRAS, 401, 791
- Springel V., 2010b, ARA&A, 48, 391
- Springel V., 2011, Invited review for the volume "Tesselations in the Sciences: Virtues, Techniques and Applications of Geometric Tilings", eds. R. van de Weijgaert, G. Vegter, J. Ritzerveld and V. Icke, astro-ph: 1109.2218
- Springel V., Farrar G. R., 2007, MNRAS, 380, 911
- Springel V., Hernquist L., 2002, MNRAS, 333, 649
- Springel V., Hernquist L., 2003a, MNRAS, 339, 289
- Springel V., Hernquist L., 2003b, MNRAS, 339, 312
- Springel V., White S. D. M., Jenkins A., Frenk C. S., Yoshida N., Gao L., Navarro J., Thacker R., Croton D., Helly J., Peacock J. A., Cole S., Thomas P., Couchman H., Evrard A., Colberg J., Pearce F., 2005, Nature, 435, 629
- Steinmetz M., White S. D. M., 1997, MNRAS, 288, 545
- Vazza F., 2011, MNRAS, 410, 461
- Vazza F., Brunetti G., Gheller C., Brunino R., 2010, New Astronomy, 15, 695
- Vazza F., Brunetti G., Gheller C., Brunino R., Brügggen M., 2011, A&A, 529, A17
- Vazza F., Dolag K., Ryu D., Brunetti G., Gheller C., Kang H., Pfrommer C., 2011, MNRAS, submitted, astro-ph: 1106.2159
- Vogelsberger M., Sijacki D., Keres D., Springel V., Hernquist L., 2011, MNRAS, submitted, astro-ph: 1109.1281
- Wadsley J. W., Veeravalli G., Couchman H. M. P., 2008, MNRAS, 387, 427
- White S. D. M., Frenk C. S., 1991, ApJ, 379, 52
- ZuHone J. A., 2011, ApJ, 728, 54

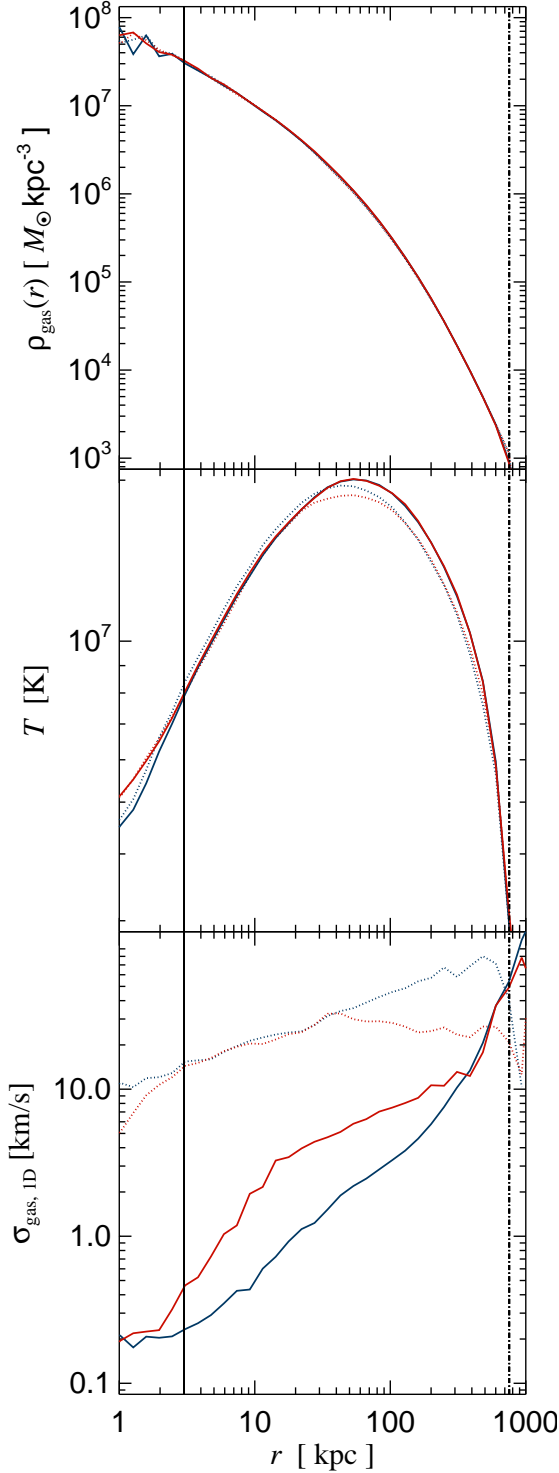


Figure A1. Radial profiles of gas density, temperature and 1D velocity dispersion at time $t = 0.05$ Gyr (dotted lines) and $t = 2.45$ Gyr (continuous lines) for GADGET (blue lines) and AREPO (red lines) with $N_{\text{gas}} = 10^6$ in a static dark matter halo with a Hernquist profile. Vertical black lines indicate the softening scales of the gas equal to $r_{\text{soft}} = 3.0$ kpc. The black vertical dot-dashed line denotes the virial radius of the system.

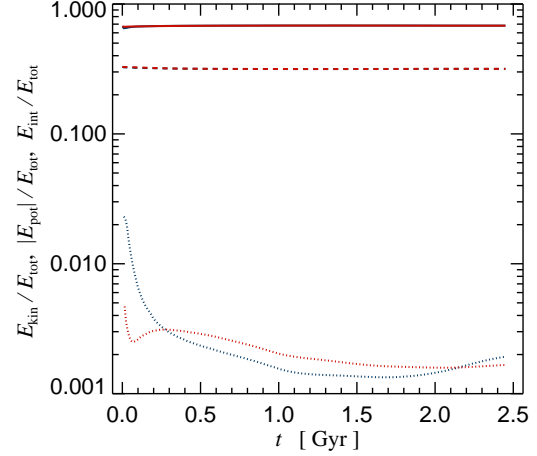


Figure A2. Time evolution of the ratio of gas kinetic (dotted lines), potential (dashed lines), and internal (continuous lines) to the total gas energy in GADGET (blue) and AREPO (red) simulations of isolated halos in hydrostatic equilibrium. Gas is self-gravitating and represented by $N_{\text{gas}} = 10^6$ resolution elements and is evolved within a static Hernquist dark matter halo.

APPENDIX A: ISOLATED HALOES IN HYDROSTATIC EQUILIBRIUM

Here we show how gaseous spheres placed in hydrostatic equilibrium within a static Hernquist dark matter halo evolve with time to determine the level of accuracy of our initial conditions. The general set-up is described in detail in Section 3.3.1. Specifically for the figures presented here we assume that the gas is self-gravitating and that it has initially zero velocity.

In Figure A1, we show gas density, temperature and 1D velocity dispersion radial profiles at $t = 0.05$ Gyr (dotted lines) and $t = 2.45$ Gyr (continuous lines) for GADGET (blue lines) and AREPO (red lines) with $N_{\text{gas}} = 10^6$ resolution elements. As discussed in Section 3.3.1, due to the Poisson sampling of the gas positions in the initial conditions they are not perfectly relaxed, which leads to the development of small-scale random motions, as evidenced by a non-zero gas velocity dispersion. Over time these residual gas velocities are dissipated, as can be seen from the bottom panel of Figure A1. This leads to a slight readjustment of the temperature distribution, which is very similar in both codes. Note, however, that the kinetic energy of the random gas motions is at all times a very small fraction of both the potential and the internal energy, as illustrated in Figure A2, amounting to only about 0.2% of the total gas energy after 2.45 Gyr.